Coupled hygrothermal and mechanical simulations of highly anisotropic building material during freezing and thawing

Fukui, Kazuma

Iba, Chiemi

Ogura, Daisuke

Coupled hygrothermal and mechanical simulations of highly anisotropic building material during freezing and thawing

Kazuma Fukui[1, *], Chiemi Iba[2], and Daisuke Ogura[3]

[1] Assistant professor, Kobe University, Graduate School of Engineering, 1-1, Rokkodai-cho, Nada-ku, Kobe 657-8501, Japan

[2] Associate professor, Kyoto University, Kyoto 615-8540, Japan

[3] Professor, Kyoto University, Kyoto 615-8540, Japan

*Corresponding author

Email: fukui@peridot.kobe-u.ac.jp

Phone: +81-78-803-6060

Nomenclature

Scalar

a	Coefficient related to the volumetric thermal expansion of pore volume occupied by each phase [K^{-1}]
c	Specific heat [J/(kg·K)]
C	Volumetric heat capacity of wet material [J/(m^3·K)]
E	Young's modulus [Pa]
E_{45}	Young's modulus in the 45° direction from the thickness direction [Pa].
G	Shear modulus [Pa]
h	Heat transfer coefficient between air and a material surface [W/(m^2·K)]
H	Latent heat of solidification (334×10^3 J/kg)
K	Bulk modulus [Pa]
m	Mass of water contained in a unit volume of bulk material [kg/m^3]
N	Biot tangent modulus [Pa]
N_{ii}, N_{il}, N_{li}, and N_l	Generalized Biot coupling modulus [Pa]
p	Pressure [Pa]
S	Saturation
T	Temperature [K],
T_m	Melting point of bulk water [K]
T_{out}	Air temperature [K]
T_r	Reference temperature [K]
α_ϕ	Coefficient related to the volumetric thermal expansion of pore volume [K^{-1}]
γ_{gl}	Surface tension between air and liquid water [N/m]
γ_{li}	Surface tension between liquid water and ice [N/m]
Δs	Melting entropy (= 1.2 MPa/K)
φ	Increment of the porosity
ϕ	Porosity
ϕ_0	Porosity in a reference state
ν	Poisson's ratio
ρ	Density [kg/m^3]
ρ^0	Density in a reference state [kg/m^3]

Tensor

$\boldsymbol{\alpha}$	Tensor of the coefficient of linear thermal expansion of a skeleton [K^{-1}]
$\mathbf{b}$	Biot tangent tensor
$\mathbf{D}$	Elastic stiffness tensor [Pa]
$\mathbf{F}$	Body force vector [N/m^3].
$\mathbf{J}$	Vectors of moisture flow [kg/(m^2·s)]
$\mathbf{n}$	Unit vector normal to the surface
$\mathbf{Q}$	Vectors of heat flow [W/m^2]
$\mathbf{t}$	External force vector [N/m^2]
$\boldsymbol{\varepsilon}$	Strain tensor
$\boldsymbol{\lambda}$	Tensor of thermal conductivity [W/(m·K)]
$\boldsymbol{\lambda}'$	Tensor of moisture permeability [kg/(m·s·Pa)]
$\boldsymbol{\sigma}$	Total stress tensor [Pa]

Subscripts

d	Bulk material in dry state
g	Water vapor
i	Ice
n	Direction normal to the thickness of a material
l	Liquid water

53	*s*	Solid phase of a material
54	*t*	Directions along the thickness of a material

55 1. Introduction

56 The freezing of porous building materials is one of the main causes of deterioration in cold
57 environments. Many studies have investigated freeze–thaw processes, damage risks, and mechanisms
58 behind deformation and damage to predict deterioration, propose proper countermeasures, and create
59 frost-resistant materials (Powers, 1945; Penttala, 1998; Scherer and Valenza II, 2005).
60 While numerous studies have experimentally investigated freeze-thaw resistance of building
61 materials, e.g., (Fagerlund, 1997; Feng, et al., 2019), numerical simulations are considered an effective
62 measure for addressing such challenges. To reveal freeze–thaw processes or evaluate frost damage
63 risks, hygrothermal models for unsaturated materials have been successfully implemented to calculate
64 the time evolution of temperature, liquid water content, and ice content distribution in building
65 materials or walls (Hokoi, et al., 2000; Matsumoto, et al., 2001; Zhou, et al., 2017; Fukui, et al., 2021a).
66 In addition, efforts have been made to develop a model with wider applications; Gawin et al. (2019)
67 proposed a model that describes non-equilibrium freezing and hysteresis of the freezing and thawing.
68 Moreover, based on the theory of poroelasticity (Biot, 1941) and poromechanics (Coussy, 2004),
69 models have been developed and widely used to predict water pressure evolution and deformation in
70 a material due to freezing (Coussy, 2005; Coussy & Monteiro, 2008; Wardeh and Perrin, 2008a;
71 Wardeh, et al., 2010; Sun and Shcerer, 2010; Zeng, et al., 2013; Gong, et al., 2015),considering various
72 mechanisms behind the development of water and ice pressure, such as pore-confined pressure,
73 hydraulic pressure (Powers, 1945), cryosuction, and crystallization pressure (Scherer, 1999). These
74 mechanical models do not consider heat and moisture movement in a material; therefore, they are used
75 for sealed specimens, specimens with small size or low water permeability, or materials with entrained
76 air in which water movement occurs locally due to sufficient pore space that allows the escape of pore
77 water.
78 Among these models, coupling models of thermal and/or moisture transfer and mechanical
79 behavior are considered powerful tools to reveal freeze–thaw processes and damage risks as well as
80 to propose proper countermeasures under various environmental conditions and combination of
81 material properties. Zuber and Marchand (2000) developed a hygro-mechanical model that was used
82 by Wardeh and Perrin (2008b) to examine the causes of pressure development in fired clay materials
83 during freezing. Zeng et al. (2011; 2016) used coupled hygrothermal and mechanical models to
84 investigate the freeze–thaw processes of cement-based materials and supercooling effects. Recently,
85 the applicability of such models has been enhanced to various problems, such as hysteresis in the
86 freeze–thaw process (Koniorczyk, 2015), pore structure changes due to cyclic freezing and thawing
87 (Koniorczyk, et al., 2015), and air-entrained effects (Eriksson, et al., 2018).
88 Porous building materials are often anisotropic, such as board materials, wood, stones, fired clay
89 materials, and bio-based materials, because of their cellular or laminated structure; the anisotropy of
90 transport properties and the strength of these materials have been investigated in the literature (Bech,
91 et al., 2003; Nguyen, et al., 2016). As geomaterials, such as rocks and soils, also exhibit anisotropy
92 either due to layered or microstructural characteristics, the theory of anisotropic poroelasticity has
93 been developed to describe the mechanical behaviors of such materials. This theory was first
94 developed by Biot (1955) and then examined by many researchers (Thompson and Willis, 1991;
95 Cheng, 1997). This approach has also been applied to building materials. Rafsanjani et al. (2015)
96 investigated the anisotropy of the swelling process of wood using a poromechanical model. Based on
97 the theory of the anisotropic poroelasticity, the material strain is determined by Biot coefficient as well
98 as stiffness tensor when the deformation is caused by pore pressure, i.e., swelling and drying, salt
99 crystallization, freezing and thawing, and so on. Therefore, the consideration of the anisotropy of Biot
100 coefficients is essential for the prediction of the stress and strain of anisotropic materials. However,
101 the freeze–thaw processes of anisotropic porous building materials have not been sufficiently
102 examined. As the poromechanical approach can potentially be applied for building wall scale (Moonen,
103 et al., 2010; Koniorczyk & Gawin, 2012; Castellazzi, et al., 2013), the mechanical behaviors of

individual materials should be properly considered to understand their interactions with other materials and behavior on a wall scale.

This study investigates prevalent numerical models for the coupled hygrothermal and mechanical behaviors of anisotropic building materials during freezing and thawing. In a previous study (Fukui, et al., 2021b), we conducted a parametric study to compare the calculation results with various combinations of Biot coefficient values. In this study, the anisotropy of the Biot coefficient is further investigated based on anisotropic poroelasticity, as well as consideration of anisotropy of the mechanical properties. First, strain measurements are reported to demonstrate the anisotropy of deformation during freezing and thawing using an ordinal brick and simulated roof tile, that have strong anisotropy of material properties. Then the calculation model which corresponded to the measurement was developed based on the conservation laws of the momentum, heat and moisture. The model was based on the poromechanics theory and included the anisotropy of the mechanical and poroelastic properties. The calculation results are then compared with the measurement results using the roof tile; moreover, the impact of the anisotropy of each material property on the anisotropy of deformation and the determinant of the magnitude of the deformation in each direction is investigated.

2. Theory of the anisotropic poroelasticity

After being established by Biot (1941), Biot himself extended the theory of poroelasticity to include anisotropic materials (Biot, 1955). Later, the constitutive relations were reinterpreted and reformed for easier application (Thompson and Willis, 1991; Cheng, 1997). In this study, the anisotropy of the Biot coefficient is estimated according to the interpretation by Cheng (1997). This interpretation is characterized by adopting micro-homogeneity and micro-isotropy assumptions to reduce the number of independent parameters necessary for calculations, which means the skeleton of porous materials is homogeneous and isotropic at microscopic scale. In the theory, the heterogeneity of the material can be attributed to the distribution of the micro homogeneous constituents and its anisotropic can be attributed to directional pores or fissure arrangement.

The generalized linear stress-strain relationship is

$$\boldsymbol{\sigma} = \mathbf{D}\boldsymbol{\varepsilon} - \mathbf{b}p \tag{1}$$

After micromechanical analysis (for more details, see (Cheng, 1997; Abousleiman and Cui, 2000)), the Biot tangent tensor for an orthotropic material can be expressed as

$$b_1 = 1 - \frac{D_{11} + D_{12} + D_{13}}{3K_s}$$

$$b_2 = 1 - \frac{D_{21} + D_{22} + D_{23}}{3K_s} \tag{2}$$

$$b_3 = 1 - \frac{D_{31} + D_{32} + D_{33}}{3K_s}$$

Building materials and geomaterials are often transverse isotropic due to the pressing, laminating, or deposition processes. For a material with its third-axis as the axis of rotational symmetry, assuming $E_1 = E_2 = E$, $E_3 = E'$, $\nu_{12} = \nu$, and $\nu_{31} = \nu_{32} = \nu'$:

$$D_{11} = D_{22} = \frac{E\left(E' - E\nu'^2\right)}{(1+\nu)\left(E' - E'\nu - 2E\nu'^2\right)}$$

$$D_{12} = D_{21} = \frac{E\left(E'\nu - E\nu'^2\right)}{(1+\nu)\left(E' - E'\nu - 2E\nu'^2\right)}$$

141 $$D_{13} = D_{23} = \frac{EE'\nu'}{E' - E'\nu - 2E\nu'^2} \quad (3)$$

142 $$D_{33} = \frac{E'^2(1-\nu)}{E' - E'\nu - 2E\nu'^2}$$

143 ## 3. Strain measurement

144 In this section, the measurements are reported using a commercial brick and simulated roof tile.

145 ### *3.1. Methods*

146 Among other building materials, fired clay materials are susceptible to frost actions. To deal with the
147 increasing risks associated with the internal insulation of masonry walls intended to improve building
148 energy efficiency (Zhou, et al., 2017; Feng, et al., 2019) and to preserve historical tiles and bricks (Iba,
149 et al., 2016), it is becoming more and more important to understand the mechanisms behind
150 deformation and damage of fired clay materials due to frost actions. Moreover, these materials are
151 known to have anisotropic properties (Stolecki, et al., 1999) and anisotropy of the cracking due to the
152 freezing has been observed (Perrin, et al., 2011).
153 In this study, two fired clay materials are employed: commercial brick and simulated roof tile. The
154 bricks are made by a local manufacturer in Aichi Prefecture, Japan. The simulated roof tile is the same
155 as that used in our previous study (Fukui, et al., 2021a). The clay commonly used for producing roof
156 tiles in this area is sintered at a temperature of 1000 °C to prepare the simulated roof tile. The material
157 is not grazed or coated to avoid spoiling its homogeneity. In addition, because the material is thin, the
158 temperature distribution during the sintering is expected small, which also contributes to its
159 homogeneity than commercial bricks. Both materials are compressed along the thickness during the
160 shaping process; therefore, they are expected to exhibit anisotropic properties and be most deformable
161 along the thickness (Stolecki, et al., 1999). The logarithmic differential pore volume distributions of
162 the two materials obtained by mercury intrusion porosimetry are shown in Fig. 1. The peak of the pore
163 volume of the brick and simulated roof tile appears at the pore diameters of 8.5 and 0.14 μm,
164 respectively, which correspond to the freezing points of −0.015 and 0.9°C, respectively (Brun, et al.,
165 1977). Additionally, the basic material and mechanical properties are listed in Table 1, showing that
166 the mechanical properties of both the materials are strongly anisotropic.
167
168 [insert Figure 1]
169

170 **Table 1.** Mechanical and some basic material properties of the two kinds of fired clay materials.

Property		Commercial brick	Simulated roof tile
Dry density		1940 kg/m^3	1800 kg/m^3
Water content at vacuum saturation (regarded as porosity)		0.246 m^3/m^3	0.299 m^3/m^3
Young's modulus	E_t	6×10^9 Pa	3×10^9 Pa
	E_n	19×10^9 Pa	11×10^9 Pa
Poisson's ratio	ν_{tn}	0.14	0.12
	ν_{nt}	0.44	0.44
	ν_{nn}	0.32	0.19

171 *Subscripts *t* and *n* represent the directions along and normal to the thickness, respectively.

A schematic of the strain measurement specimens is presented in Fig. 2. Specimens with the original material thickness (approximately 60 and 20 mm for the brick and simulated roof tile, respectively) are used. The specimens are rectangles with a bottom surface of 59.8 mm × 206.1 mm and 46.4 mm × 94.7 mm, and a height of 98.1 mm and 21.0 mm for the brick and simulated roof tile, respectively. The height of the specimen corresponds to the material thickness. Strain gauges and thermocouples are attached to the center of the top surface and to one of the 98.1 mm × 206.1 mm and 21.0 mm × 94.7 mm sides of the commercial brick and roof tile specimens, respectively using cyanoacrylate adhesive. The strain gauges employed are KFLB-5-120-C1-11 R3M3 (Kyowa Electronic Instruments Co., Ltd). The strain is measured normal to and along the height on the top and side surfaces, respectively, to confirm the anisotropy of deformation during freezing and thawing. Due to the complexity to govern the equilibrium relationship among the three phases (air, liquid water, and ice) in the numerical simulations, the specimens were fully (vacuum-)saturated during the experiment for easier comparison. After attaching the strain gauges and thermocouples and saturating the specimen in a vacuum, the specimen is loosely covered with a thin plastic wrap to hinder surface vaporization but not to restrict the expansion of the specimen, allowing liquid water movement thorough the surfaces. The thermal resistance of the wrap is confirmed negligible prior to the experiment. The specimen is placed on a mesh to minimize thermal and mechanical interactions due to direct contact with the test chamber. In addition, the specimen is covered with a mesh basket to prevent direct exposure to the wind in the chamber.

[insert Figure 2]

To stabilize the distribution of the temperature in the specimen, the temperature of the air inside the test chamber with the specimen is first maintained at 20 °C for 30 min. The set temperature is then changed in a stepwise manner and maintained at −20 °C and 20 °C for 4 h during the cooling and heating periods, respectively, for the simulated roof tile. However, the minimum temperature is set to −10 °C for the commercial brick specimen due to the restrictions of experimental devices. From the pore volume distribution (shown in Fig. 1) and expected freezing temperature, this temperature is sufficient to freeze most of the pore water in the brick specimen. Considering the higher minimum temperature and larger dimensions of the commercial brick specimen, the cooling and heating periods are prolonged to 21 h and 15 h, respectively. The strain and temperature of the specimen are recorded every second during the experiment as well as the temperature of the air in the chamber.

3.2. Results

The measured time evolution of the temperature and strain of the specimens during the freeze–thaw experiments are shown in Figs. 3. Figure 4 displayed the measured strain changes as a function of the temperature. The strain evolutions on both the top and side surfaces (normal to and along the thickness, respectively) are presented in Figs. 3 and 4, but the temperature is not shown on the top surface in Fig. 3 as the evolutions of temperature at the two measuring points are similar. The strain is shown referring to the values at 20 °C during the cooling process. In Fig. 3 (a), there is a sudden rise of the air temperature in the chamber at the elapsed time of 18 h due to open of the door of the test chamber to check the condition inside.

[insert Figure 3]
[insert Figure 4]

For the roof tile, the surface temperature once decreased to −4.8 °C and then suddenly increased due to the freezing of the supercooled water during an early stage of the cooling period. Then the measured temperature of both of the two materials stopped decreasing at sub-zero temperature due to the release of the latent heat. At the same time, the strain in the thickness direction of both of the materials start increasing.

The measurement results indicate that the strain along the thickness of both the materials significantly increases as the temperature decreases below 0 °C. In the direction normal to the

thickness, the commercial brick specimen contracts and then expands as the temperature decreased. This expansion is faster than that along the thickness, but the magnitude is significantly smaller. After the elapsed time of 12h, the increase of the strain in both directions stopped, which indicated most of the freezable water solidified at this moment. From these results, the anisotropy of the deformation of the brick due to the frost action was confirmed.

Moreover, the simulated roof tile demonstrates the stronger anisotropy of deformation due to frost actions. It expanded more significantly in the thickness direction that the brick, but negligibly expands in the direction normal to the thickness and rather contracts.

4. Numerical simulation

In this section, the hygrothermal and mechanical simulations are described based on the theory of poromechanics. Herein, the simulated roof tile is selected as the object of calculation. The material has a significantly strong anisotropy in its mechanical properties and simple dimensions, which allows the use of a simple assumption in predicting the poroelastic properties that are not measured for general building materials.

4.1. Methods

4.1.1. Constitutive equations

Constitutive equations are based on the theory of poromechanics.

$$\boldsymbol{\sigma} = \mathbf{D}\left[\boldsymbol{\varepsilon} - \boldsymbol{\alpha}\left(T - T_r\right)\right] - \mathbf{b}p \tag{4}$$

$$\varphi = \mathbf{b} : \boldsymbol{\varepsilon} + \frac{p}{N} - \alpha_\phi \left(T - T_r\right) \tag{5}$$

When pores contain ice and liquid water, equations (4) and (5) are expressed as

$$\boldsymbol{\sigma} = \mathbf{D}\left[\boldsymbol{\varepsilon} - \boldsymbol{\alpha}\left(T - T_r\right)\right] - \left(\mathbf{b_i} p_i + \mathbf{b_l} p_l\right) \tag{6}$$

$$\varphi_i = \mathbf{b_i} : \boldsymbol{\varepsilon} + \frac{p_i}{N_{ii}} + \frac{p_l}{N_{il}} - a_i\left(T - T_r\right) \qquad \varphi_l = \mathbf{b_l} : \boldsymbol{\varepsilon} + \frac{p_i}{N_{li}} + \frac{p_l}{N_{ll}} - a_l\left(T - T_r\right) \tag{7}$$

Coussy (2005) and Coussy & Monteiro (2008) expressed $\mathbf{b_i}$ and $\mathbf{b_l}$ in equations (6) and (7) as values proportional to the ice and liquid water saturation, respectively, i.e.,

$$\mathbf{b_j} = \mathbf{b} S_j \qquad j = i, l \tag{8}$$

In addition, the anisotropy of $\boldsymbol{\alpha}$ is ignored considering thermal effects on the deformation was not significant compared with the water pressure development during the freezing; therefore, the thermal expansion coefficient of the material is represented by one value, α. The final forms of the constitutive equations are

$$\boldsymbol{\sigma} = \mathbf{D}\left[\boldsymbol{\varepsilon} - \alpha\left(T - T_r\right)\mathbf{I}\right] - \mathbf{b}\left(S_i p_i + S_l p_l\right) \tag{9}$$

$$\varphi_i = S_i \mathbf{b} : \boldsymbol{\varepsilon} + \frac{p_i}{N_{ii}} + \frac{p_l}{N_{il}} - a_i\left(T - T_r\right) \qquad \varphi_l = S_l \mathbf{b} : \boldsymbol{\varepsilon} + \frac{p_i}{N_{li}} + \frac{p_l}{N_{ll}} - a_l\left(T - T_r\right) \tag{10}$$

The poroelastic parameters a_j, $\mathbf{b}$, N_{ji}, and N_{jl} in equations (9) and (10) are to be given, but $\mathbf{b}$ can be calculated using equation (2) following the Cheng's assumption when K_s is obtained. As it is difficult to fully determine the set of the poroelastic parameters from the measurement, we approximate these values considering the strong anisotropy of the material. Considering the laminated structure of the material, it is assumed to have parallel pores which were vertical to the thickness direction. This assumption leads to a relationship $E_s = E_n / (1 - \phi)$ and $\nu_s = \nu_{nn}$. K_s is then obtained using the relationship $K_s = E_s / (3 (1 - 2\nu_s))$. Next, the equations derived by Aichi and Tokunaga (2011) are used to obtain N_{ji} and N_{jl}. It is assumed that the Young's modulus along the thickness of the material is significantly smaller than that in the direction normal to the thickness ($E_t << E_n$) or that the deformation in the normal direction is considerably smaller than that along the thickness. We obtain

$$\frac{1}{N_{ll}} \approx \frac{b_t - \phi_0}{E_s} S_l^2 \quad \frac{1}{N_{li}} = \frac{1}{N_{il}} \approx \frac{b_t - \phi_0}{E_s} S_l S_i \quad \frac{1}{N_{ii}} \approx \frac{b_t - \phi_0}{E_s} S_i^2 \tag{11}$$

The derivation of a_j has not been reported for anisotropic materials in (Coussy, 2004). Since the anisotropy of the thermal expansion coefficient of solid volume is ignored in this study, the thermal expansion of pore volume is assumed to be isotropic. Therefore, a_j is derived assuming isotropy (Coussy, 2004), as

$$a_j = 3\alpha \left(b_t - \phi_0\right) S_j \qquad j = i, l \tag{12}$$

Finally, the main simplifications used in the aforementioned equations can be summarized as follows:

- Plastic deformation of the material is ignored.
- As expressed in equation (8), $\mathbf{b_i}$ and $\mathbf{b_l}$ are set to values proportional to the saturation S (Coussy, 2005; Coussy and Monteiro, 2008).
- The anisotropy of the thermal expansion coefficient α is ignored.
- The poroelastic parameters a_j, N_{ji}, and N_{jl} are given in simplified forms. This is reasonable because the simulated roof tile exhibits strong anisotropy.

4.1.2. Equilibrium relationship between ice and liquid water

The Clausius–Clapeyron equation is expressed (Coussy and Monteiro, 2009) as

$$\frac{p_l}{\rho_l} - \frac{p_i}{\rho_i} = \frac{\Delta s}{\rho_i} \left(T - T_m\right) \tag{13}$$

To express the dependencies of water density on the pressure p of each phase and temperature T, linearized form (Coussy, 2005; Coussy and Monteiro, 2008) is used as

$$\frac{1}{\rho_j} = \frac{1}{\rho_j^0} \left(1 - \frac{p_j}{K_j} + 3\alpha_j \left(T - T_r\right)\right) \qquad j = i, l \tag{14}$$

Liquid water saturation S_l is obtained from the difference between ice pressure p_i and liquid water pressure p_l under thermodynamic equilibrium conditions. The model as suggested by van Genuchten (1980) is

$$S_l = \left[\frac{1}{1 + \left(\beta \left(p_i - p_l\right)\right)^n}\right]^m \tag{15}$$

where m, n, and β are fitting parameters.

The difference in the shape of the interface between ice and liquid water causes hysteresis during freezing and thawing (Koniorczyk, et al., 2015; Gawin, et al., 2019). However, the freezing and

thawing processes are not distinguished in the calculation, i.e., the hysteresis is ignored, assuming that it does not strongly affect the directionality of deformation.

4.1.3. Conservation equations

The momentum balance and conservation equations for the heat and moisture mass are expressed as

$$\nabla \cdot \boldsymbol{\sigma} + \mathbf{F} = 0 \tag{16}$$

$$\frac{\partial}{\partial t}\left(CT - Hm_i\right) = \nabla \cdot \left(\boldsymbol{\lambda} \nabla T\right) \tag{17}$$

$$\frac{\partial}{\partial t}\left(m_i + m_l\right) = \nabla \cdot \left(\boldsymbol{\lambda}' \nabla p_l\right) \tag{18}$$

where

$$C = c_d \rho_d + c_i m_i + c_l m_l \tag{19}$$

Note that $\mathbf{F} = 0$ because no source of the external force is considered

4.1.4. Calculation model, numerical solution, and calculation conditions

Figure 5 presents the calculation model corresponding to the strain measurements described in the previous section. The calculation is performed two-dimensionally to examine the relationship of the strain in the two directions. The three-dimensional effects were not considered to reduce the calculation cost given that the material is long and the heat and moisture transfer in the direction of the long sides of the bottom surfaces is not dominant. The calculated region was on a quarter of a 40 mm × 20 mm cross-section (shown with a black square in Fig. 5), provided that the specimen is symmetric. The direction of the 20-mm sides corresponds to the direction along the material thickness. A plane-strain state is assumed as the strain in the depth direction was not significant. The *x*- and *y*-axes of the rectangular coordinate system are set in the directions of the 40- and 20-mm sides, respectively (shown in Fig. 5). The discretization of the conservation equations with respect to space is performed using the Galerkin finite element method based on the monolithic approach, and 2 mm × 2 mm bilinear elements are used. The calculation results do not depend on the mesh size as confirmed by comparing the calculation results using elements with half sides. Vectors of nodal values $\mathbf{T_e}$, $\mathbf{p_e}$, and $\mathbf{u_e}$ are used to express temperature T, liquid water pressure p_l, and displacement vector $\mathbf{u}$, respectively as well as the shape functions $\mathbf{N}$ and $\mathbf{N_u}$ as

$$T = \mathbf{N}\mathbf{T_e} \quad p_l = \mathbf{N}\mathbf{p_e} \quad \mathbf{u} = \mathbf{N_u}\mathbf{u_e} \tag{20}$$

After discretization, the following system are obtained

$$\begin{bmatrix} \mathbf{C_{TT}} & \mathbf{C_{Tp}} & \mathbf{C_{Tu}} \\ \mathbf{C_{pT}} & \mathbf{C_{pp}} & \mathbf{C_{pu}} \\ \mathbf{C_{uT}} & \mathbf{C_{up}} & \mathbf{C_{uu}} \end{bmatrix} \frac{\partial}{\partial t} \begin{bmatrix} \mathbf{T_e} \\ \mathbf{p_e} \\ \mathbf{u_e} \end{bmatrix} = \begin{bmatrix} \mathbf{K_{TT}} & \mathbf{0} & \mathbf{0} \\ \mathbf{0} & \mathbf{K_{uu}} & \mathbf{0} \\ \mathbf{0} & \mathbf{0} & \mathbf{0} \end{bmatrix} \begin{bmatrix} \mathbf{T_e} \\ \mathbf{p_e} \\ \mathbf{u_e} \end{bmatrix} + \begin{bmatrix} \mathbf{f_T} \\ \mathbf{f_p} \\ \partial \mathbf{f_u} / \partial t \end{bmatrix} \tag{21}$$

where equation (16) is differentiated based on time. Components in equation (21) are presented in the appendix. The finite difference method is used to discretize the basic equations with respect to time with a backward difference. The time step is set to 1 s.

[insert Figure 5]

The initial and boundary conditions are listed in Table 2. The initial temperature of the material is set to a uniform value, and the average of the temperatures at the two measuring points at the beginning of the freeze–thaw experiment is used. The initial liquid water pressure p_l for the material is assumed to be 0 Pa as the specimen is vacuum saturated at the beginning of the experiment. On the symmetry axes (x = 0 or y = 0 in Fig. 5), the displacement is restricted normal to the axis directions and no heat or moisture flow is given. The surface vaporization is prevented by plastic wrap during the experiment; however, the wrap is not stiff and not considered to restrict movement of liquid water through the surfaces. Therefore, liquid water pressure p_l on the material surface is assumed to be 0 Pa. The heat flow through the surfaces is calculated using the Robin boundary condition and the measured air temperature in the test chamber. A stress-free boundary condition is assumed on the surfaces of the material. The thermal transfer coefficient h is set to 6.5 [W/(m^2·K)] for the calculated temperature changes to agree with the measurement results.

Table 2. Initial and boundary conditions of the calculation.

	Position	Coordinates (shown in Fig. 5)	Heat	Moisture	Stress and displacement
Initial conditions	Calculation area	$0 \le x \le L_x$ and $0 \le y \le L_y$	Measured temperature	$p_l = 0$	$\mathbf{u} = 0$
Boundary conditions	Axes of symmetry	$x = 0$ or $y = 0$	$\mathbf{Q}\cdot\mathbf{n} = 0$	$\mathbf{J}\cdot\mathbf{n} = 0$	$\mathbf{u}\cdot\mathbf{n} = 0$
	Material surfaces	$x = L_x$ or $y = L_y$	$\mathbf{Q}\cdot\mathbf{n} = h\,(T - T_{out})$	$p_l = 0$	$\boldsymbol{\sigma}\cdot\mathbf{n} = 0$

4.1.5. Hygrothermal and mechanical properties

The properties of the simulated roof tile with constant values necessary for the calculations, dry density, porosity, specific heat, thermal expansion coefficient, Young's modulus, and Poisson's ratio are listed in Table 3. The thermal expansion coefficient α is determined from the slope of the strain as a function of the temperature above 0 °C in Fig. 4 (b). The table includes the anisotropy of the Young's modulus, and Poisson's ratio. The shear modulus G of the material is calculated as (Hayashi, 1954)

$$\frac{1}{G} = \frac{4}{E_{45}} - \left(\frac{1}{E_t} + \frac{1}{E_n} - \frac{\nu_{tn}}{E_t} \right) \tag{22}$$

It is assumed that E_{45} is the average of E_t and E_n.

Table 3. Material properties of the simulated roof tile with constant values.

Property	Unit	Symbol	Value	Source
Dry density	kg/m^3	ρ_d	1800	(Fukui, et al., 2021a)
Water content at vacuum saturation (regarded as porosity)	m^3/m^3	ϕ_0	0.299	(Fukui, et al., 2021a)
Specific heat	J/(kg·K)	c_d	840	(Kumaran, 1996)
Thermal expansion coefficient	K^{-1}	α	4.8×10^{-6}	Measurement
Young's modulus	Pa	E_t	3×10^9	Measurement
		E_n	11×10^9	Measurement
Poisson's ratio		ν_{tn}	0.12	Measurement
		ν_{nt}	0.44	Measurement
		ν_{nn}	0.19	Measurement

For simplicity, the anisotropy of the thermal conductivity is ignored as it does not significantly affect the directionality of the deformation. Measurements are performed on specimens with various S_l values using the transient hot-wire method. From the results, the relationship between S_l and λ is obtained as (Fukui, et al., 2021a)

$$\lambda = 1.26 S_l + 0.55 \tag{23}$$

Additionally, the Maxwell equation, referring to de Vries (1963), is used to apply equation (23) to the freezing and thawing processes as (Fukui, et al., 2021a)

$$\lambda = 1.26 S_l + 2.15 S_i + 0.55 \tag{24}$$

Here the equation in the literature was rewritten using the saturation degree instead of the volumetric water content.

The moisture retention curve of the material is obtained using the gas absorption and pressure plate methods (Fukui, et al., 2021a). Figure 6(a) presents the measurement results and fitted curve. For the fitted curve, the form suggested by van Genuchten (1980) is used as

$$S_l = \left[1 + \left(\beta \left(p_g - p_l \right) \right)^n \right]^{-m} \tag{25}$$

The parameters in the equation are determined as follows: $m = 0.57$, $n = 2.3$, and $\beta = 1.12 \times 10^{-6}$ Pa^{-1}. Using the calibrated parameters, the liquid water saturation of the saturated material during freezing and thawing is calculated considering the difference in the interfacial energy between the water vapor and liquid water and between the liquid water and ice, as (Zeng, et al., 2011)

$$S_l = \left[1 + \left(\beta' \left(p_i - p \right) \right)^n \right]^{-m} \tag{26}$$

where $\beta' = (\gamma_{gl} / \gamma_{li}) \times \beta$ [Pa^{-1}]. As stated earlier, the hysteresis during the freeze–thaw processes is ignored.

[insert Figure 6]

During the experiment, the water in the specimen is expected to move towards the surfaces from the inside of the specimen due to the pressure development induced by freezing. Consequently, the water pressure in the specimen can be relaxed to some extent. Therefore, the moisture transfer properties of the material are considered important for predicting freezing strain. The water diffusivity D in the direction normal to the material thickness is obtained using the Boltzmann transformation

from time evolution of the water content distribution during water uptake measured using the gamma-ray attenuation method (Fukui, 2021a). As the material is thin such that the moisture profile along the thickness cannot be obtained using the same, mass measurements are performed during water uptake to compare the average D (Kumaran 1999) along and normal to the thickness. From the results, the average D is 2.1 times lesser along the thickness than in the direction normal to the thickness. Next, D in the entire saturation range is assumed 2.1 times smaller along the thickness. The λ' calculated from D and the water retention curve are presented in Fig. 6 (b) along with the fitted curve.

4.1.6. Poroelastic properties and calculation cases

The values of the Biot coefficient calculated from equation (2) with the Young's modulus and Poisson's ratio listed in Table 3 are 0.679 and 0.219 along and normal to the thickness, respectively. Therefore, not only the Young's modulus and Poisson's ratio but also the Biot coefficient of this material are strongly anisotropic.

In equations (6) and (7), the anisotropy of the material strain is determined by the stiffness tensor and Biot coefficient. Therefore, the anisotropy of the Young's modulus, Poisson's ratio, and Biot coefficients has broad effects on the evolution of the material strain. The following three calculations are conducted to examine the effects of each property.

- For Case 1, only the anisotropy of water permeability is considered.
- For Case 2, the anisotropy of Young's modulus and Poisson's ratio is considered as well as that of the water permeability.
- For Case 3, the anisotropy of the Biot coefficient is considered as well as that of the water permeability, Young's modulus, and Poisson's ratio.

These three cases are summarized in Table 4. When the isotropy of the Biot coefficients, Young's modulus, and Poisson's ratio are assumed, the properties in the thickness directions are applied in all the directions (values are provided in Table 3). Note that the anisotropy of the water permeability is considered in all of the calculation cases because the property is related to the significance of the pressure development and deformation, but the other material properties are assumed isotropic.

Table 4 The consideration of anisotropic properties in each calculation case

	Young's modulus	Poisson's ratio	Biot coefficient
Case 1	Isotropy*	Isotropy*	Isotropy*
Case 2	Anisotropy	Anisotropy	Isotropy*
Case 3	Anisotropy	Anisotropy	Anisotropy

*The properties in the thickness directions are applied in all directions.

4.2. Results

Figures 7 and 8 present the results of the calculation of Case 1, as well as the measured temperature and strain evolution, respectively. The strain evolution on both the top and side surfaces (normal to and along the thickness, respectively) is presented in Fig. 8, but the temperature is not shown on the top surface in Fig. 7 as the evolutions of temperature at the two measuring points are similar. Below 0 °C, the calculated strain along the thickness increases as the temperature decreases, same as the measured strain. The difference in the magnitude of the calculated and measured evolutions of the strain may be due to the inaccuracy in material properties, such as the moisture diffusivity and water retention curve (These properties are related to the rate of the solidification and the water escape toward the surfaces of the material due to the pressure development and consequently affect the magnitude of the deformation. For example, smaller moisture diffusivity prevents moisture movement when the pressure increases due to the freezing, which induces more significant pressure rise and strain. Consequently, the agreement between the measurement and calculation will become better.) In addition, the changes in the mechanical properties due to the water content changes (Fukui et al., 2019)

or evolution in the plastic strain can attribute to the difference between the measured and calculated results. However, the trend in the measured strain change is well reproduced in the calculation.

[insert Figure 7]
[insert Figure 8]

For Case 1, the calculated strain in the direction normal to the thickness also increases and completely disagrees with the measurement results that decrease during freezing. Therefore, the mechanically and poroelasitically isotropic models are insufficient for reproducing the measured results.

Next, Figs 9 and 10 present the results of Cases 2 and 3. The calculated strain along the thickness and the temperature do not significantly change from those in Case 1 (the temperature is not shown in this paper). Although the strain change in the direction normal to the thickness during freezing in Case 2 (shown in Fig. 9) is smaller than that in Case 1, the material still expands in this direction. The material contracts in this direction in Case 3 in which the anisotropy of the Biot coefficient is considered, which is consistent with the measured results.

[insert Figure 9]
[insert Figure 10]

4.3. Discussion

In this section we compare the contribution of the temperature changes, water pressure development, and Poisson's effects to the strain evolution based on the calculation results where the anisotropy of the Young's modulus, Poisson's ratio, and Biot coefficient is considered, and analyze the dominant sources of the deformation in each direction of the material. First, thermal contraction due to the temperature changes during the freeze-thaw cycle along and normal to the thickness is determined based on the calculated temperature evolution as

$$\varepsilon_{tt}^{T} = \varepsilon_{nn}^{T} = \alpha\left(T - T_r\right) \tag{27}$$

Here we ignored the anisotropy of the thermal expansion coefficient. T_r is the set value of the initial temperature (20 °C). Next, the strain change due to water (liquid water and ice) pressure development in the material (excluding Poisson's effects) is obtained based on the calculated ice and liquid water saturation and pressure as

$$\varepsilon_{tt}^{H} = \frac{b_t}{E_t}\left(S_i p_i + S_l p_l\right) \quad \varepsilon_{nn}^{H} = \frac{b_n}{E_n}\left(S_i p_i + S_l p_l\right) \tag{28}$$

Finally, the Poisson's effects due to the expansion associated with water pressure development in the vertical direction are considered as

$$\varepsilon_{tt}^{P} = -\frac{\nu_{tn} b_n}{E_t}\left(S_i p_i + S_l p_l\right) \quad \varepsilon_{nn}^{P} = -\frac{\nu_{nt} b_t}{E_n}\left(S_i p_i + S_l p_l\right) \tag{29}$$

As no external force was considered in the calculations, these three factors are main determinant of the deformation of the material.

Using equations (27) to (29) with the calculated temperature, water saturation, and pressure evolution in Case 3, the strain due to the thermal contraction, hydrostatic pressure, and Poisson's effect were calculated. Figure 11 shows comparison of the contribution of these causes of the deformation to the strain evolution. Due to the restriction of the deformation from the neighborhood elements, the sum of the strain caused by the three causes is not consistent perfectly with the calculated overall strain shown in Fig. 10. However, it seems that they mainly determine the magnitude and trend

of the deformation. From Fig. 11 (a), the expansion along the thickness is mainly attributed to the increase in the hydrostatic pressure in the material due to freezing; moreover, the thermal contraction and Poisson's effects are almost negligible. In contrast, Fig. 11 (b) shows that the three components of strain evolution compete in the direction normal to the thickness. The expansion associated with the hydrostatic pressure development is suppressed due to the small Biot coefficient and large Young's modulus in this direction, while the Poisson's effect is dominant because of the large expansion along the thickness. According to these results, the contribution of the water pressure rise in pores to the deformation of the specimen is relatively small in the direction normal to the thickness compared with the contribution of the Poisson effect accompanied by the expansion along the thickness. This resulted in the contraction of the material in the direction normal to the thickness. Therefore, a model that only considers the anisotropy of the general mechanical properties (Case 2) cannot reproduce such a contraction, and the anisotropy of the Biot coefficients should be adequately considered.

[insert Figure 11]

5. Conclusion

In this study, the effects of anisotropy of the material properties on the deformation during freezing and thawing processes and proper numerical modeling of it are investigated. The strain measurement using two fired clay materials confirmed the strongly anisotropic deformation during the freezing. Notably, the plate-shaped simulated roof tile contracted in the direction normal to the thickness while it expanded significantly in the thickness direction. The freeze–thaw process is then simulated based on theory of poromechanics and anisotropic poroelasticity. The comparison between the measured and calculated results reveals that applying only the anisotropy of mechanical properties is insufficient for reproducing the anisotropic deformation of the material; moreover, the contraction in the direction normal to the thickness can be reproduced only when the anisotropies of the Biot coefficient and general mechanical properties are considered. Analysis of the causes of the deformation reveals that the expansion in the direction normal to the thickness due to the pressure development during the freezing is suppressed by the large Young's modulus and small Biot coefficient and the contraction due to the Poisson's effects accompanied by the large expansion in the thickness direction can be a dominant factor of the deformation in the direction normal to the thickness. Therefore, considering the anisotropy of the Biot coefficient is recommended when materials with laminated structures, such as types of stones and fired clay materials, are considered.

In this study, we chose the simulated roof tile as the target of the calculations considering its relatively simple dimensions, small heterogeneity, and strong anisotropy in the mechanical properties due to the laminated structure or orientation of particles compared with bricks, which allowed us to predict the poroelastic properties under simple assumptions of parallel pore structure. In the future, the deformation of bricks, which also exhibited the anisotropy in the strain measurement will be further explored for the practical application. In addition, the validity of such assumptions for other types of building materials needs further investigation for a wider application of anisotropic poroelasticity to various building materials

Appendix

The components in equation (21) are defined as

$$\mathbf{C}_{\mathbf{TT}} = \int_{\Omega} \frac{\partial}{\partial T}\left(CT - H_{li} m_i\right) \mathbf{N}^T \mathbf{N} d\Omega \tag{A.1}$$

$$\mathbf{C}_{\mathbf{Tp}} = \int_{\Omega} \frac{\partial}{\partial p_l}\left(CT - H m_i\right) \mathbf{N}^T \mathbf{N} d\Omega \tag{A.2}$$

$$\mathbf{C}_{\mathbf{Tu}} = \int_{\Omega} \frac{\partial}{\partial \varepsilon_v} \left(CT - Hm_i \right) \mathbf{N}^T \mathbf{m}^T \mathbf{B} d\Omega \tag{A.3}$$

$$\mathbf{C}_{\mathbf{pT}} = \int_{\Omega} \frac{\partial}{\partial T} \left(m_i + m_l \right) \mathbf{N}^T \mathbf{N} d\Omega \tag{A.4}$$

$$\mathbf{C}_{\mathbf{pp}} = \int_{\Omega} \frac{\partial}{\partial p_l} \left(m_i + m_l \right) \mathbf{N}^T \mathbf{N} d\Omega \tag{A.5}$$

$$\mathbf{C}_{\mathbf{pu}} = \int_{\Omega} \frac{\partial}{\partial \varepsilon_v} \left(m_i + m_l \right) \mathbf{N}^T \mathbf{m}^T \mathbf{B} d\Omega \tag{A.6}$$

$$\mathbf{C}_{\mathbf{uT}} = -\int_{\Omega} \left[\alpha \mathbf{B}^{\mathbf{T}} \mathbf{D} + b \frac{\partial}{\partial T} \left(S_i p_i + S_l p_l \right) \mathbf{B}^{\mathbf{T}} \right] \mathbf{m} \mathbf{N} d\Omega \tag{A.7}$$

$$\mathbf{C}_{\mathbf{up}} = -\int_{\Omega} b \frac{\partial}{\partial p_l} \left(S_i p_i + S_l p_l \right) \mathbf{B}^{\mathbf{T}} \mathbf{m} \mathbf{N} d\Omega \tag{A.8}$$

$$\mathbf{C}_{\mathbf{uu}} = \int_{\Omega} \mathbf{B}^{\mathbf{T}} \mathbf{D} \mathbf{B} d\Omega \tag{A.9}$$

$$\mathbf{K}_{\mathbf{TT}} = \int_{\Omega} \nabla \mathbf{N}^T \boldsymbol{\lambda} \nabla \mathbf{N} d\Omega + \int_{\Gamma} h \mathbf{N}^T d\Gamma \tag{A.10}$$

$$\mathbf{K}_{\mathbf{pp}} = \int_{\Omega} \nabla \mathbf{N}^T \boldsymbol{\lambda}' \nabla \mathbf{N} d\Omega \tag{A.11}$$

$$\mathbf{f}_{\mathbf{T}} = -\int_{\Gamma} \left(Q - hT_{out} \right) \mathbf{N}^T d\Gamma \tag{A.12}$$

$$\mathbf{f}_{\mathbf{P}} = -\int_{\Gamma} J \mathbf{N}^T d\Gamma \tag{A.13}$$

$$\frac{\partial \mathbf{f}_{\mathbf{u}}}{\partial t} = \frac{\partial}{\partial t} \int_{\Gamma} \mathbf{N}_{\mathbf{u}}{}^T \mathbf{t} d\Gamma \tag{A.14}$$

where Ω and Γ are the domains of an element and its boundary, respectively; moreover,

$$\mathbf{m} = \begin{bmatrix} 1 & 1 & 0 \end{bmatrix}^T \tag{A.15}$$

$$\mathbf{B} = \begin{bmatrix} \frac{\partial N_1}{\partial x_1} & 0 & \frac{\partial N_2}{\partial x_1} & 0 & \frac{\partial N_3}{\partial x_1} & 0 & \frac{\partial N_4}{\partial x_1} & 0 \\ 0 & \frac{\partial N_1}{\partial x_2} & 0 & \frac{\partial N_2}{\partial x_2} & 0 & \frac{\partial N_3}{\partial x_2} & 0 & \frac{\partial N_4}{\partial x_2} \\ \frac{\partial N_1}{\partial x_2} & \frac{\partial N_1}{\partial x_1} & \frac{\partial N_2}{\partial x_2} & \frac{\partial N_2}{\partial x_1} & \frac{\partial N_3}{\partial x_2} & \frac{\partial N_3}{\partial x_1} & \frac{\partial N_4}{\partial x_2} & \frac{\partial N_4}{\partial x_1} \end{bmatrix} \tag{A.16}$$

References

Abousleiman, Y. & Cui, L., 2000. The theory of anisotropic poroelasticity with applications. In: *Modeling in Geomechanics.* New York: Wiley, pp. 559-93.

Aichi, M. & Tokunaga, T., 2011. Thermodynamically consistent anisotropic constitutive relations for a poroelastic material saturated by two immiscible fluids. *International Journal of Rock Mechanics & Mining Sciences,* Volume 48, pp. 580-84.

Bech, K., Al-Mukhtar, M., Rozenbaum, O. & Rautureau, M., 2003. Characterization, water transfer properties and deterioration in tuffeau: building material in the Loire valley—France. *Building and Environment,* Volume 38, pp. 1152-62.

Biot, M. A., 1941. General theory of three-dimensional consolidation. *Journal of Applied Physics,* Volume 12, pp. 155-64.

Biot, M. A., 1955. Theory of elasticity and consolidation for a porous anisotropic solid. *Journal of Applied Physics,* Volume 26, pp. 182-85.

Brun, M., Lallemand, A., Quinson, J. & Eyraud, C., 1977. A new method for the simultaneous determination of the size and the shape of pores: the thermoporometry. *Thermochimica Acta,* Volume 21, pp. 59-88.

Castellazzi, G. et al., 2013. A coupled multiphase model for hygrothermal analysis of masonry structures and prediction of stress induced by salt crystallization. *Construction and Building Materials,* Volume 41, pp. 717-31.

Cheng, A. H.-D., 1997. Material coefficients of anisotropic poroelasticity. *International Journal of Rock Mechanics & Mining Sciences,* Volume 34, pp. 199-205.

Coussy, O., 2004. *Poromechanics.* s.l.:John Wiley & Sons.

Coussy, O., 2005. Promechanics of freezing materials. *Journal of the Mechanics and Physics of Solids,* Volume 53, pp. 1689-1718.

Coussy, O. & Monteiro, P. J., 2008. Poroelastic model for concrete exposed to freezing temperatures. *Cement and Concrete Research,* Volume 38, pp. 40-48.

Coussy, O. & Monteiro, P. J., 2009. Errata to 'Poroelastic model for concrete exposed to freezing temperatures'. *Cement and Concrete Research,* Volume 39, pp. 371-72.

de Vries, D. A., 1963. Thermal properties of soils. In: *Physics of Plant Environment.* Amsterdam: North-Holland Publishing Corporation, pp. 210-35.

Eriksson, D., Gasch, T., Malm, R. & Ansell, A., 2018. Freezing of partially saturated air-entrained concrete: A multiphase description of the hygro-thermo-mechanical behaviour. *International Journal of Solids and Structures,* Volume 152-53, pp. 294-304.

Fagerlund, G., 1997. *Internal frost attack-state of the art: suggestions for future research (Report TVBM (Intern 7000-rapport); Vol. 7110),* Division of Building Materials, LTH, Lund University.

Feng, C., Roels, S. & Janssen, H., 2019. Towards a more representative assessment of frost damage to porous building materials. *Building and Environment,* Volume 164, p. 106343.

Fukui, K. et al., 2021a. Investigation into the hygrothermal behavior of fired clay materials during the freezing of supercooled water using experiments and numerical simulations. *Journal of Building Physics,* p. https://doi.org/10.1177/17442591211041144.

Fukui, K., Chiemi, I., Daisuke, O., 2021b. Effects of anisotropy of properties of fired clay materials on strain evolution and results of coupled hygrothermal and mechanical simulations during freezing and thawing. In: *8the International Building Physics Conference*, Copenhagen, Denmark, 25-27 August 2021.

Gawin, D., Pesavento, F., Koniorczyk, M. & Schrefler, B. A., 2019. Non-equilibrium modeling hysteresis of modeling hysteresis of thawing in partially saturated porous building materials. *Journal of Building Physics,* Volume 43, pp. 61-98.

Gong, F., Sicat, E., Zhang, D. & Ueda, T., 2015. Stress analysis for concrete materials under multiple freeze-thaw cycles. *Journal of Advanced Concrete Technology,* Volume 13, pp. 124-34.

Hayashi, T., 1954. On the elastic properties of an orthogonal-anisotropic plate having the proncipal axes of elasticity slanted to its edges. *Journal of the Japan Society of Aeronautical Engineering,* Volume 2, pp. 12-17.

Hokoi, S., Hatano, M., Matsumoto, M. & Kumaran, M. K., 2000. Freezing-Thawing Processes in Glass Fiber Board. *Journal of Thermal Envelope and Building Science,* Volume 24, pp. 42-60.

578 Iba, C., Ueda, A. & Hokoi, S., 2016. Field survey on frost damage to roof tiles under climatic
579 conditions. *Structural Survey,* Volume 34, pp. 135-49.
580 Koniorczyk, M., 2015. Coupled heat and water transport in deformable porous materials considering
581 phase change kinetics. *International Journal of Heat and Mass Transfer,* Volume 81, pp. 260-71.
582 Koniorczyk, M. & Gawin, D., 2012. Modelling of salt crystallization in building materials with
583 microstructure - Poromechanical approach. *Construction and Building Materials,* Volume 36, pp.
584 860-73.
585 Koniorczyk, M., Gawin, D. & Schrefler, B. A., 2015. Modeling evolution of frost damage in fully
586 saturated porous materials exposed to variable hygro-thermal conditions. *Computer Methods in*
587 *Applied Mechanics and Engineering,* Volume 297, pp. 38-61.
588 Kumaran, M. K., 1996. *IEA Annex 24, Final Report, Vol. 3, Task 3: Material Properties.* Leuven:
589 Laboratorium Boufysica, Department Burgerlijke Bouwkunde, KU Leuven.
590 Kumaran, M. K., 1999. Moisture diffusivity of building materials from water absorption measurements.
591 *Journal of Thermal Envelope and Building Science,* Volume 22, pp. 349-55.
592 Penttala, V., 1998. Freezing-induced strains and pressures in wet porous materials
593 Matsumoto, M., Hokoi, S. & Hatano, M., 2001. Model for simulation of freezing and thawing
594 processes in building materials. *Building and Environment,* Volume 36, pp. 733-42.
595 Moonen, P., Sluys, L. J. & Carmeliet, J., 2010. A continuous-discontinuous approach to simulate
596 physical degradation process in porous media. *International Journal for Numerical Methods in*
597 *Engineering,* Volume 84, pp. 1009-37.
598 Nguyen, S. T. et al., 2016. Modeling thermal conductivity of hemp insulation material: A multi-scale
599 homogenization approach. *Building and Environment,* Volume 107, pp. 127-34.
600 Penttala, V., 1998. Freezing-induced strains and pressures in wet porous materials and especially in
601 concrete mortars. *Advanced Cement Based Materials,* Volume 7, pp. 8-19.
602 Perrin, B. et al., 2011. Mechanical behaviour of fired clay materials subjected to freeze–thaw cycles.
603 *Construction and Building Materials,* Volume 25, pp. 1056-64.
604 Powers, T. C., 1945. A working hypothesis for further studies of frost resistance of concrete. *Journal*
605 *of the American Concrete Institute,* Volume 16, pp. 245-72.
606 Rafsanjani, A., Derome, D. & Carmeliet, J., 2015. Poromechanical modeling of moisture induced
607 swelling anisotropy in cellular tissues of softwoods. *RSC Advances,* Volume 5, pp. 3560-66.
608 Scherer, G. W., 1999. Crystallization in pores. *Cement and Concrete Research,* Volume 29, pp. 1347-
609 58.
610 Scherer, G. W. & Valenza II, J. J., 2005. Mechanisms of frost damage. In: *Materials Science of*
611 *Concrete VII.* s.l.:American Ceramic Society, pp. 209-46.
612 Stolecki, J., Piekarczyk, J. & Rudnik, T., 1999. Heterogenity and anisotropy of ceramic roof tiles.
613 *British Ceramic Proceedings,* Volume 60, pp. 383-84.
614 Sun, Z. & Shcerer, G. W., 2010. Effects of air voids on salt scaling and internal freezing. *Cement and*
615 *Concrete Research,* Volume 40, pp. 260-70.
616 Thompson, M. & Willis, J. R., 1991. A reformation of the equations of anisotropic poroelasticity.
617 *Journal of Applied Mechanics,* Volume 58, pp. 612-16.
618 Van Genuchten, M. T., 1980. A Closed-form Equation for Predicting the Hydraulic Conductivity of
619 Unsaturated Soils. *Soil Science Society of America Journal,* Volume 44, pp. 892-98.
620 Wardeh, G., Mohamed, M. A. & Ghorbel, E., 2010. Analysis of concrete internal deterioration due to
621 frost action. *Journal of Building Physics,* Volume 35, pp. 54-82.
622 Wardeh, G. & Perrin, B., 2008a. Numerical modelling of the behaviour of consolidated porous media
623 exposed to frost action. *Construction and Building Materials,* Volume 22, pp. 600-08.
624 Wardeh, G. & Perrin, B., 2008b. Freezing–thawing phenomena in fired clay materials and
625 consequences on their durability. *Construction and Building Materials,* Volume 22, pp. 820-28.
626 Zeng, Q., Fen-Chong, T., Dangla, P. & Li, K., 2011. A study of freezing behavior of cementitious
627 materials by poromechanical approach. *International Journal of Solids and Structures,* Volume 48,
628 pp. 3267-73.
629 Zeng, Q., Fen-Chong, T. & Li, K., 2013. Elastic behavior of saturated porous materials under
630 undrained freezing. *Acta Mechanica Sinica,* Volume 29, pp. 827-35.

631 Zeng, Q., Li, K. & Fen-Chong, T., 2016. Effect of supercooling on the instantaneous freezing dilation
632 of cement-based porous materials. *Journal of Building Physics,* Volume 40, pp. 101-24.
633 Zhou, X., Derome, D. & Carmeliet, J., 2017. Hygrothermal modeling and evaluation of freeze-thaw
634 damage risk of masonry walls retrofitted with internal insulation. *Building and Environment,*
635 Volume 125, pp. 285-98.
636 Zuber, B. & Marchand, J., 2000. Modeling the deterioration of hydrated cement systems exposed to
637 frost action Part 1: Description of the mathematical model. *Cement and Concrete Research,*
638 Volume 30, pp. 1929-39.
639

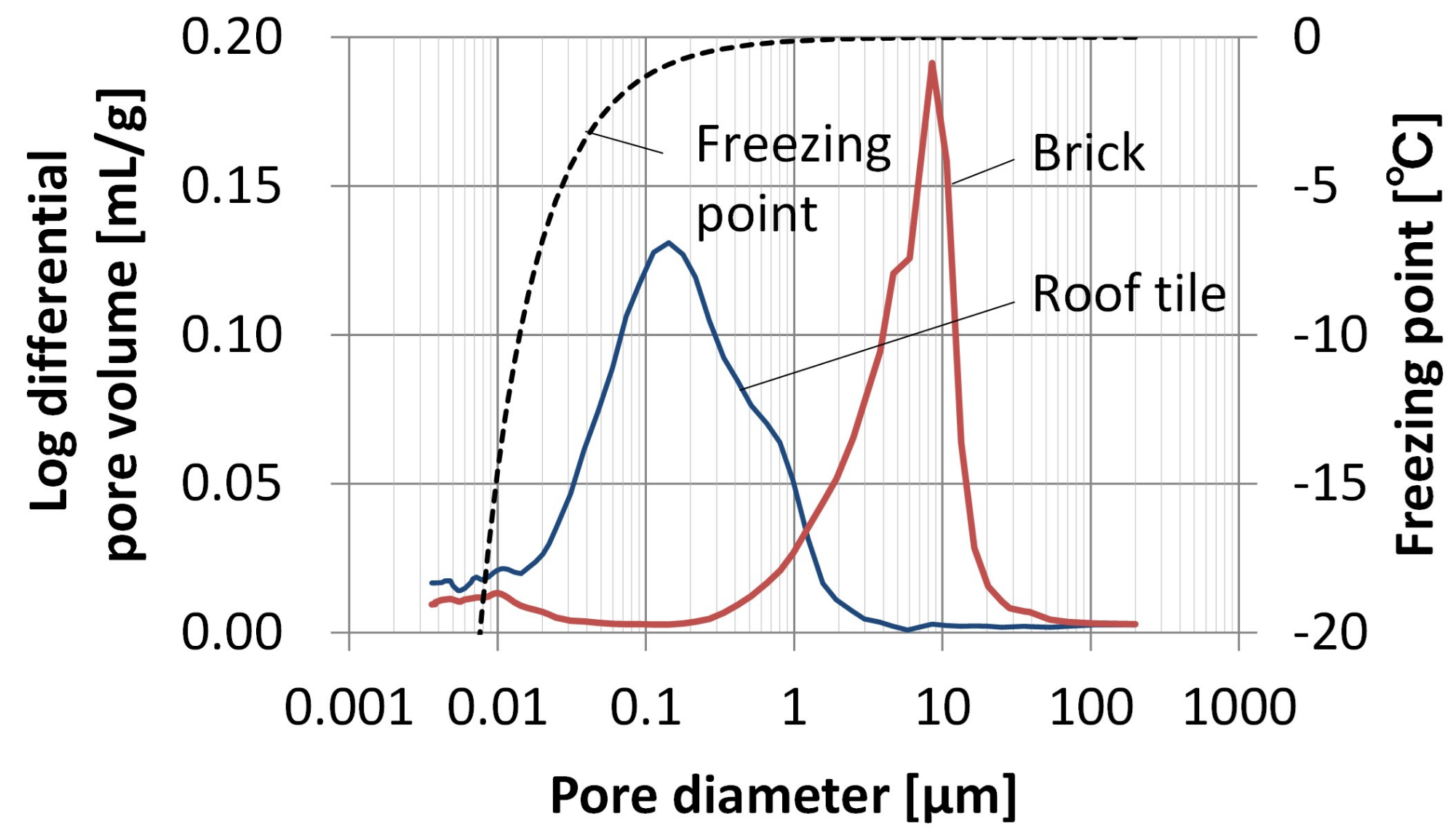
Log differential pore volume [mL/g]
0.20
0.15
0.10
0.05
0.00
Freezing point [°C]
0
-5
-10
-15
-20
Freezing point
Brick
Roof tile
0.001
0.01
0.1
1
10
100
1000
Pore diameter [µm]

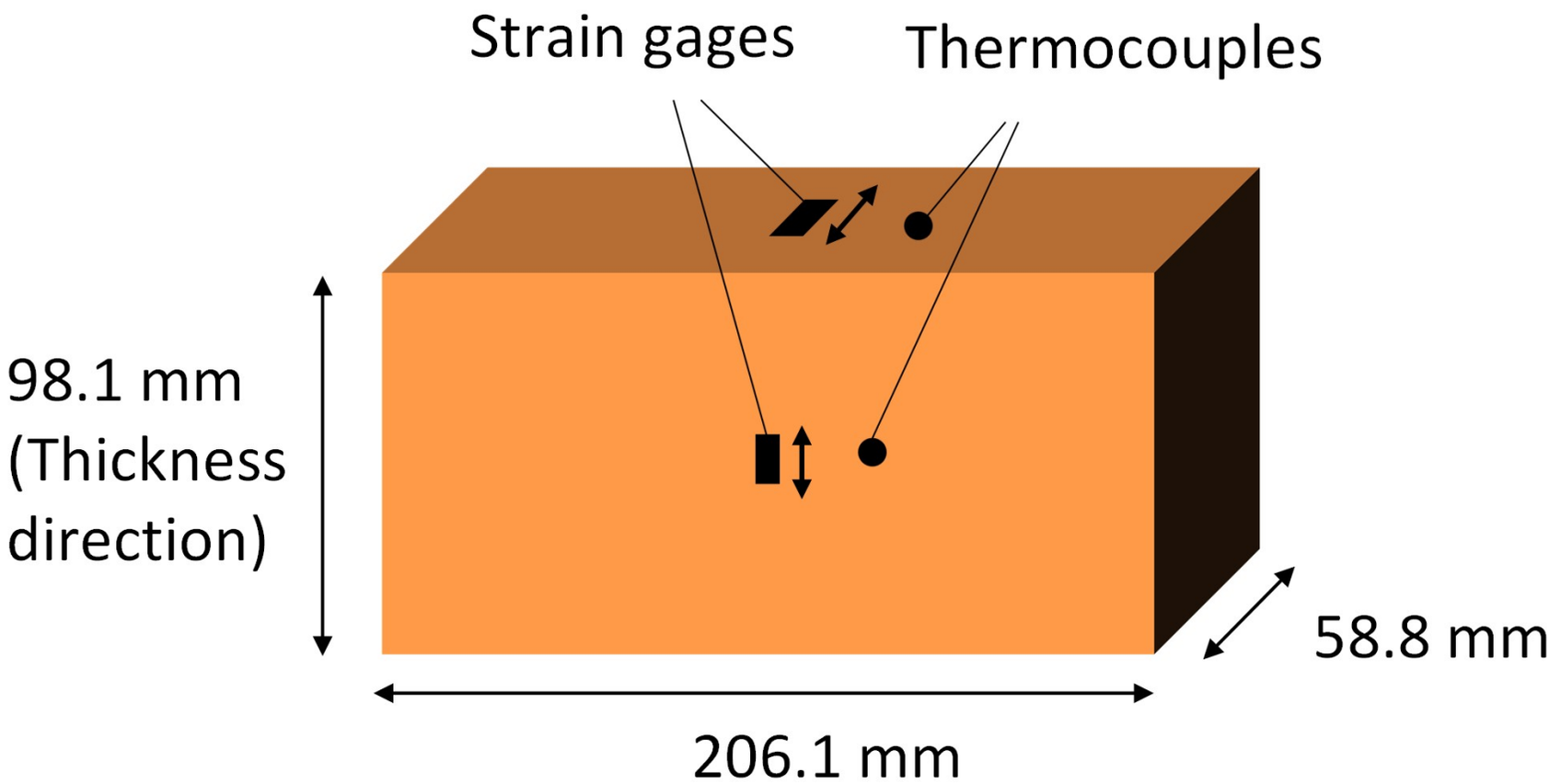
Strain gages
Thermocouples
98.1 mm
(Thickness
direction)
58.8 mm
206.1 mm

(a)

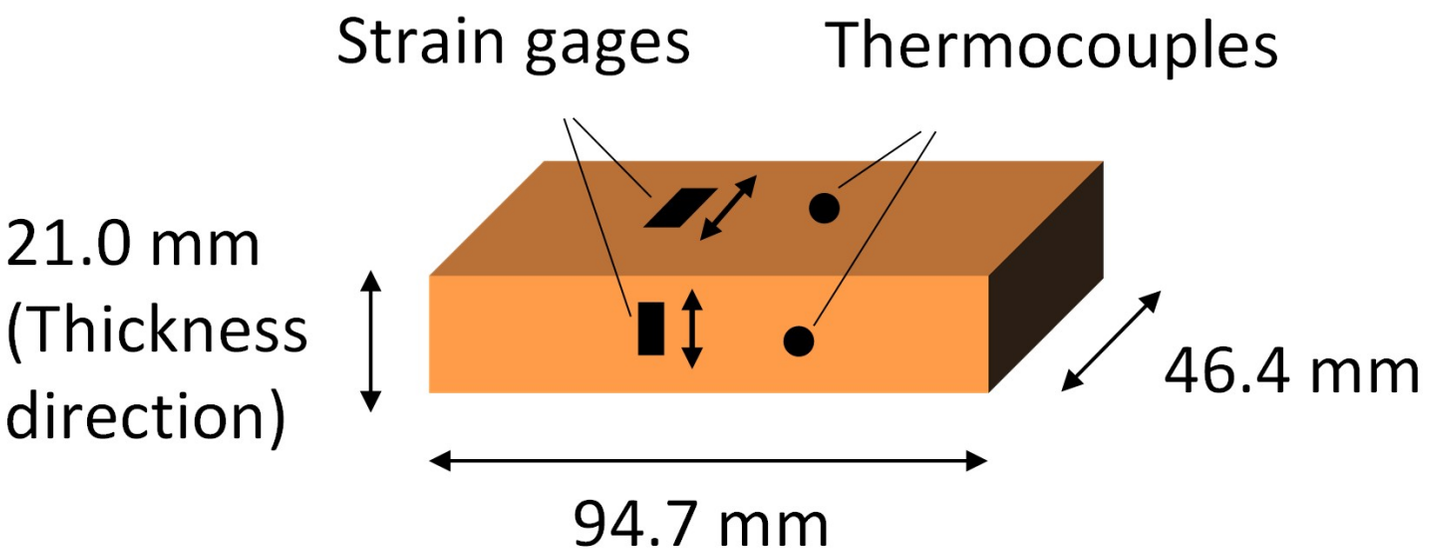
Strain gages
Thermocouples
21.0 mm
(Thickness
direction)
46.4 mm
94.7 mm

(b)

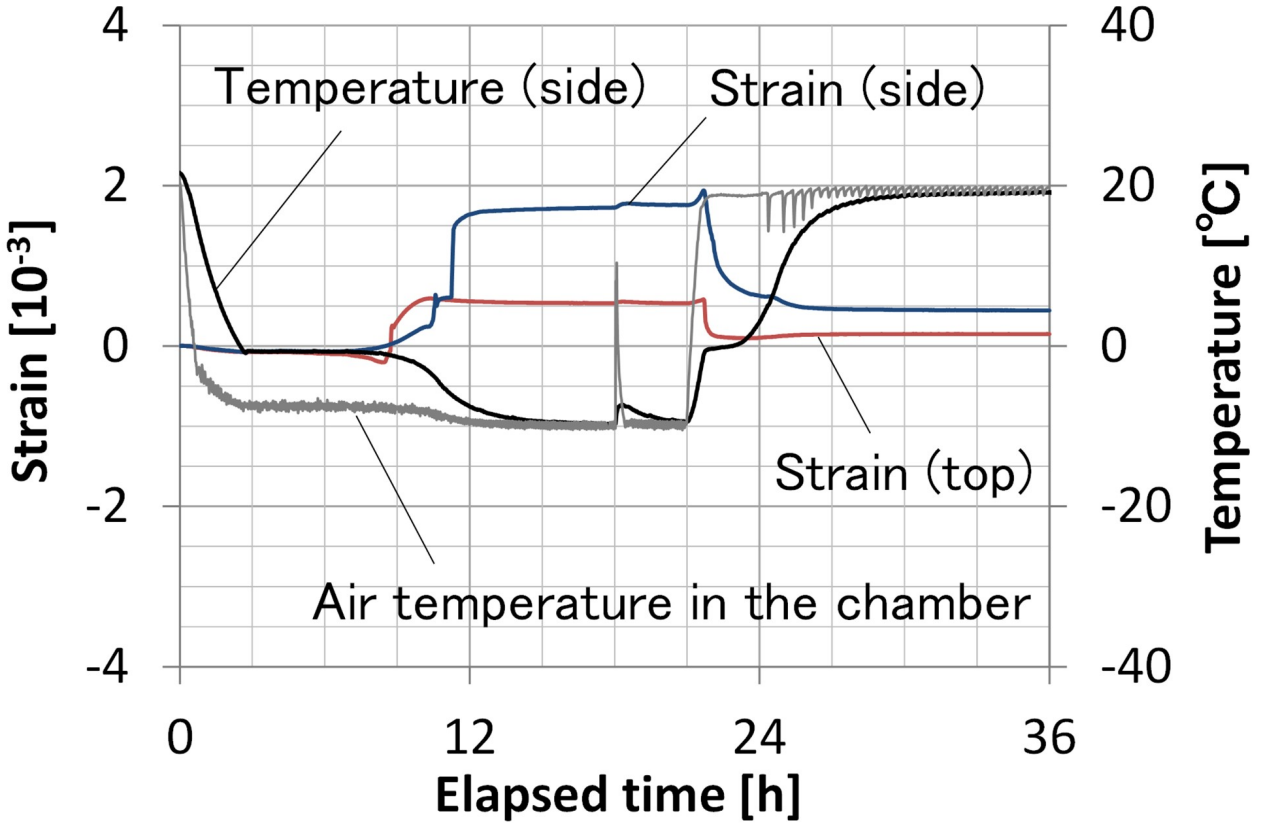
Temperature (side)
Strain (side)
Strain (top)
Air temperature in the chamber
Strain [10-3]
Temperature [°C]
Elapsed time [h]
4
2
0
-2
-4
40
20
0
-20
-40
0
12
24
36

(a)

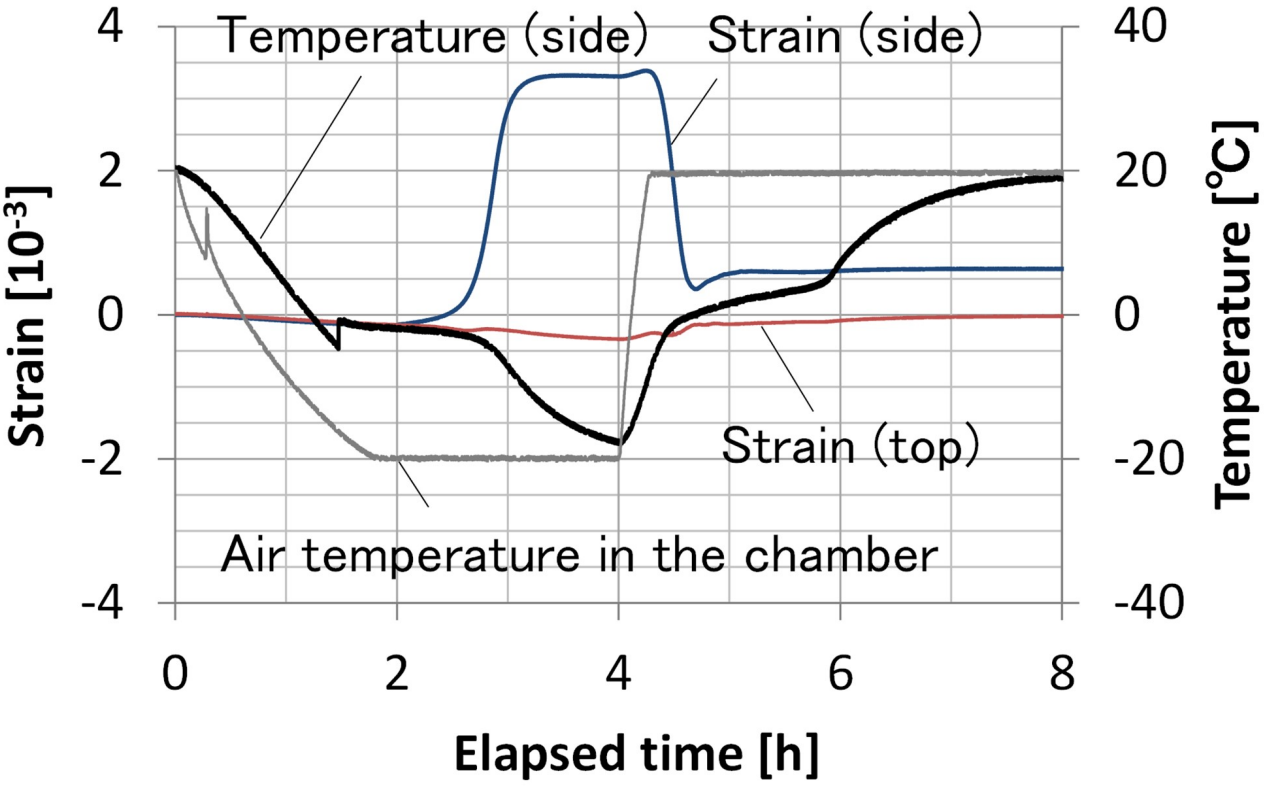
Temperature (side)
Strain (side)
Strain (top)
Air temperature in the chamber
Strain [10-3]
Temperature [°C]
Elapsed time [h]
4
2
0
-2
-4
40
20
0
-20
-40
0
2
4
6
8

(b)

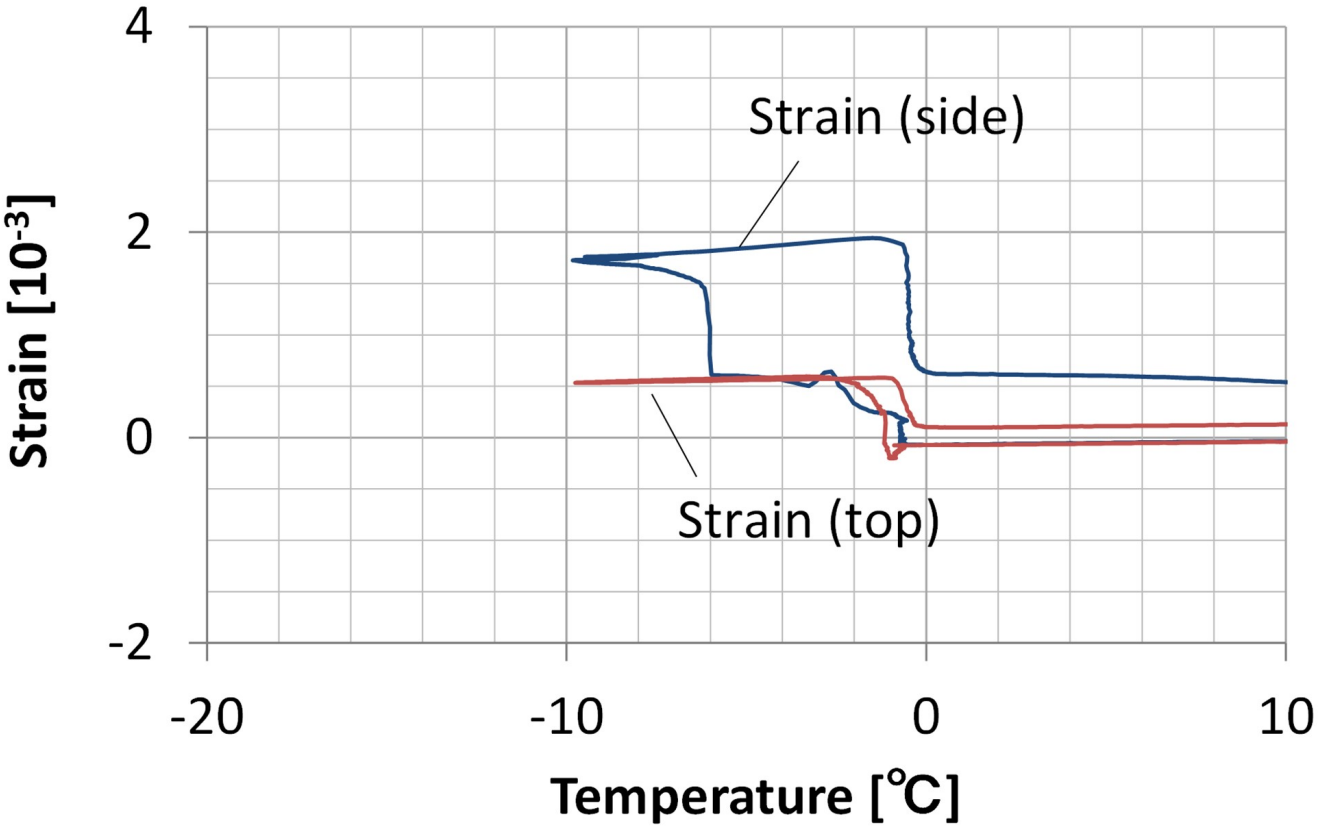
Strain (side)
Strain (top)
Strain [10-3]
Temperature [℃]
4
2
0
-2
-20
-10
0
10

(a)

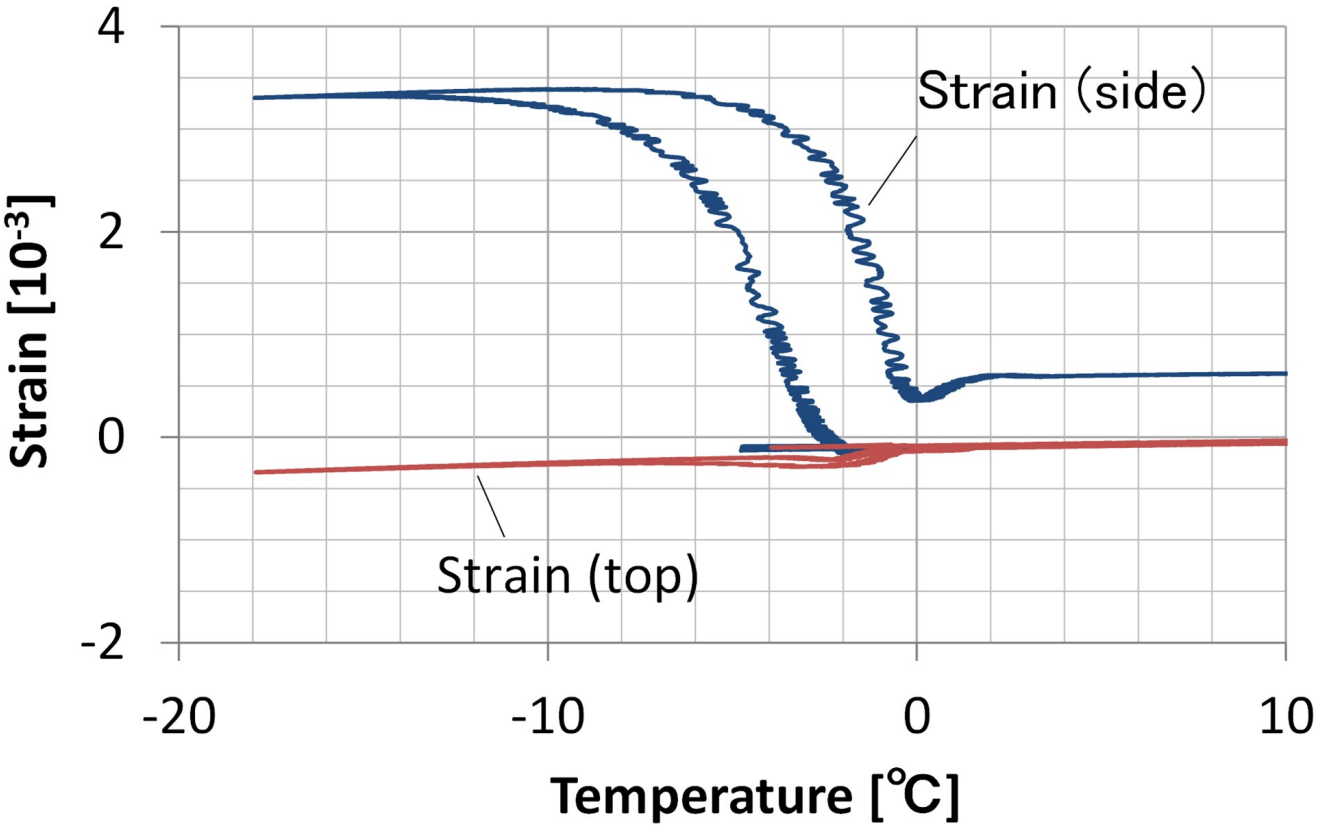
Strain (side)
Strain (top)
Strain [10-3]
Temperature [℃]
4
2
0
-2
-20
-10
0
10

(b)

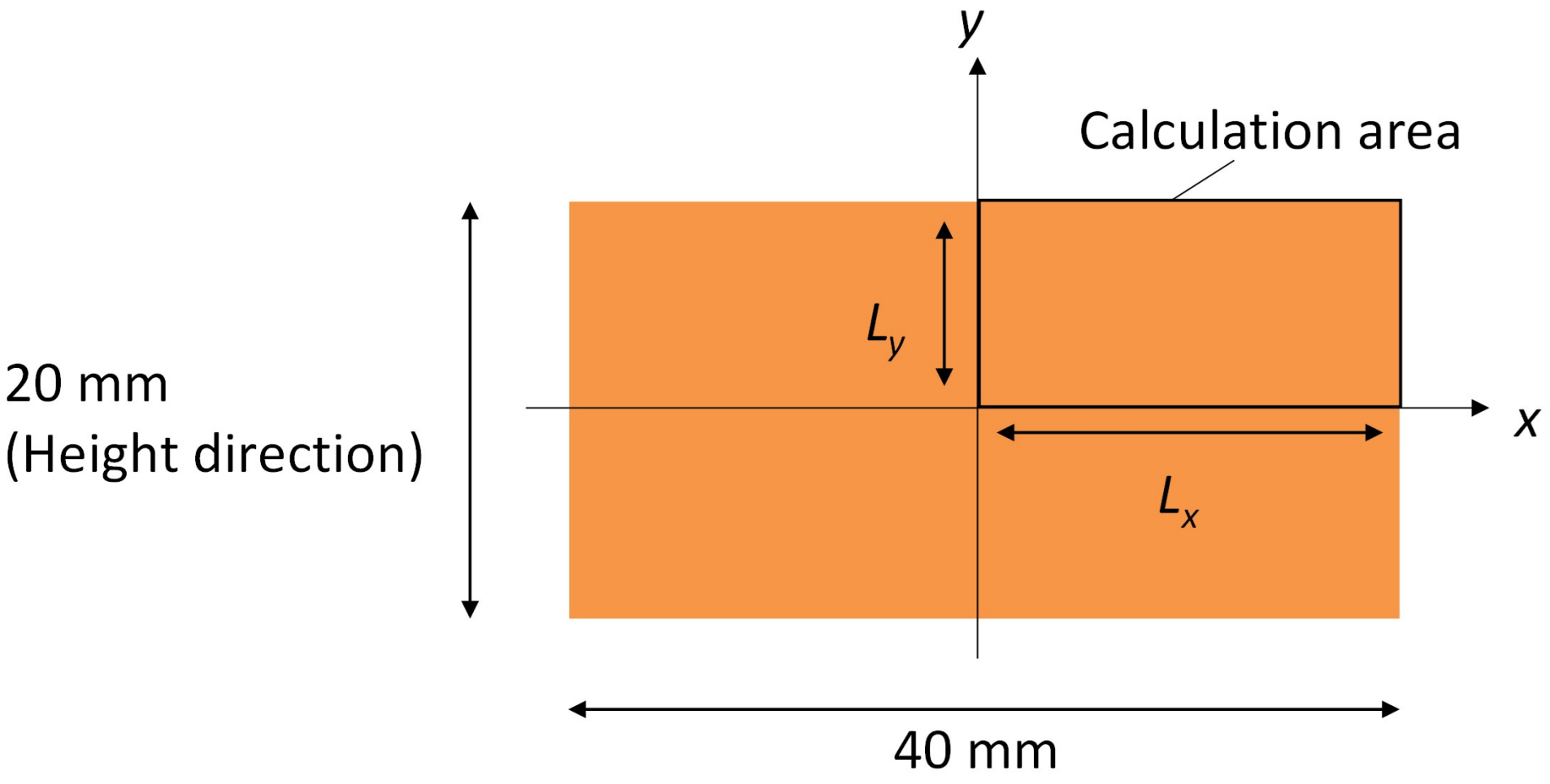
y
Calculation area
L_y
x
L_x
20 mm
(Height direction)
40 mm

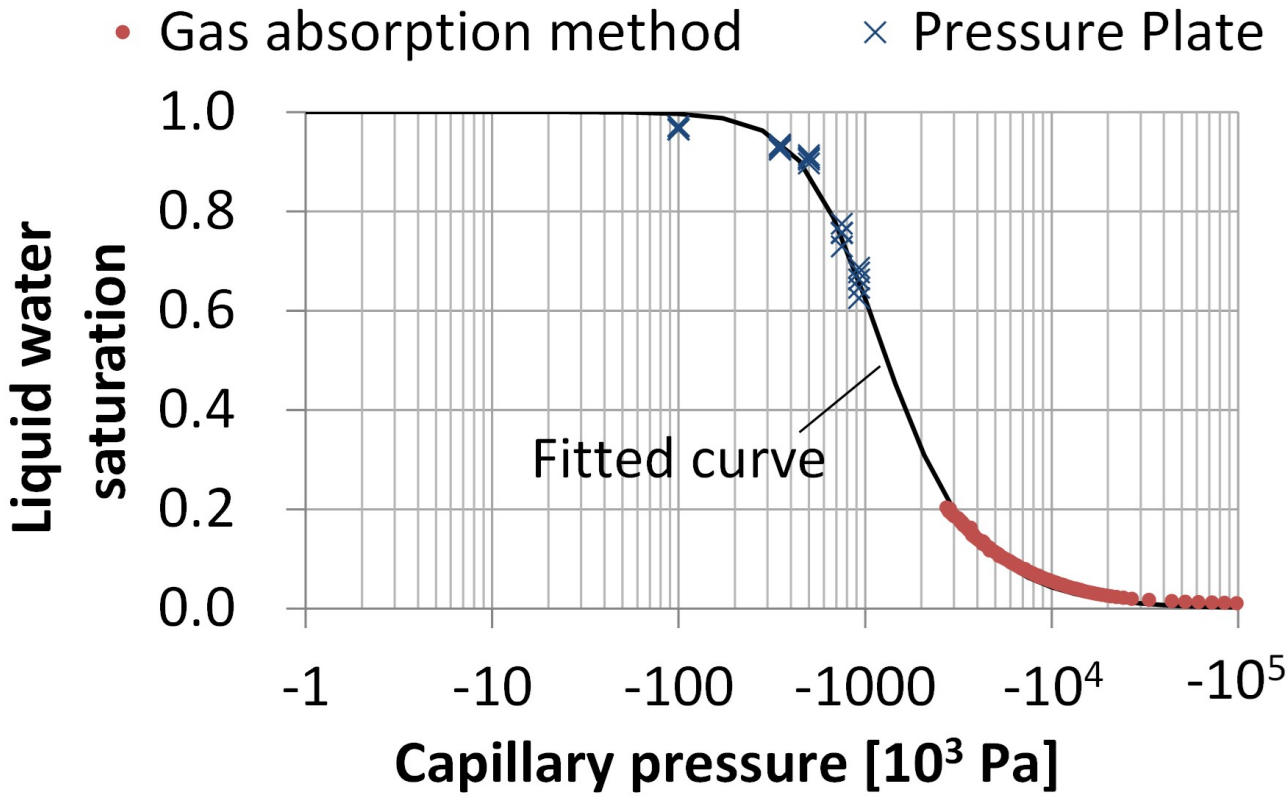
Gas absorption method
Pressure Plate
Liquid water saturation
1.0
0.8
0.6
0.4
0.2
0.0
Fitted curve
-1
-10
-100
-1000
-10^4
-10^5
Capillary pressure [10^3 Pa]

(a)

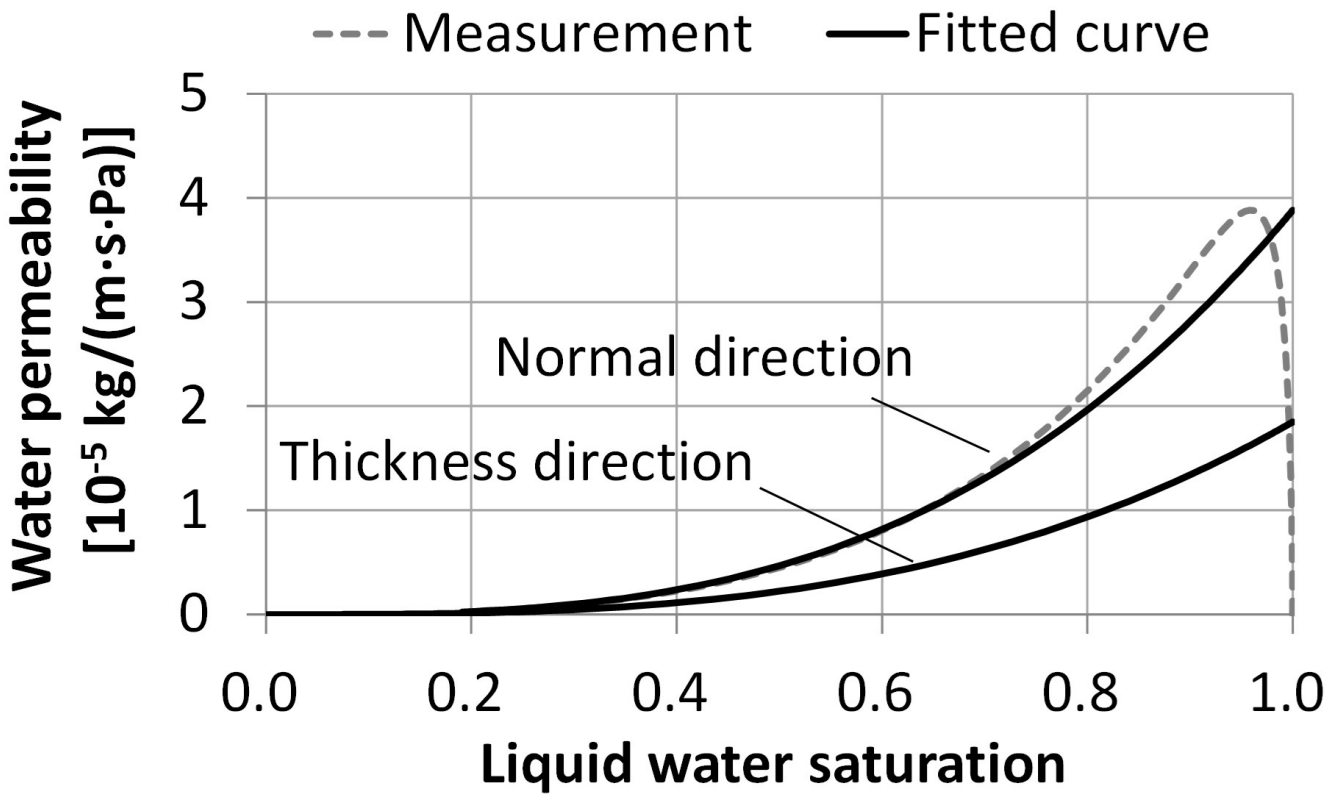
Measurement
Fitted curve
Water permeability [10^-5 kg/(m·s·Pa)]
5
4
3
2
1
0
Normal direction
Thickness direction
0.0
0.2
0.4
0.6
0.8
1.0
Liquid water saturation

(b)

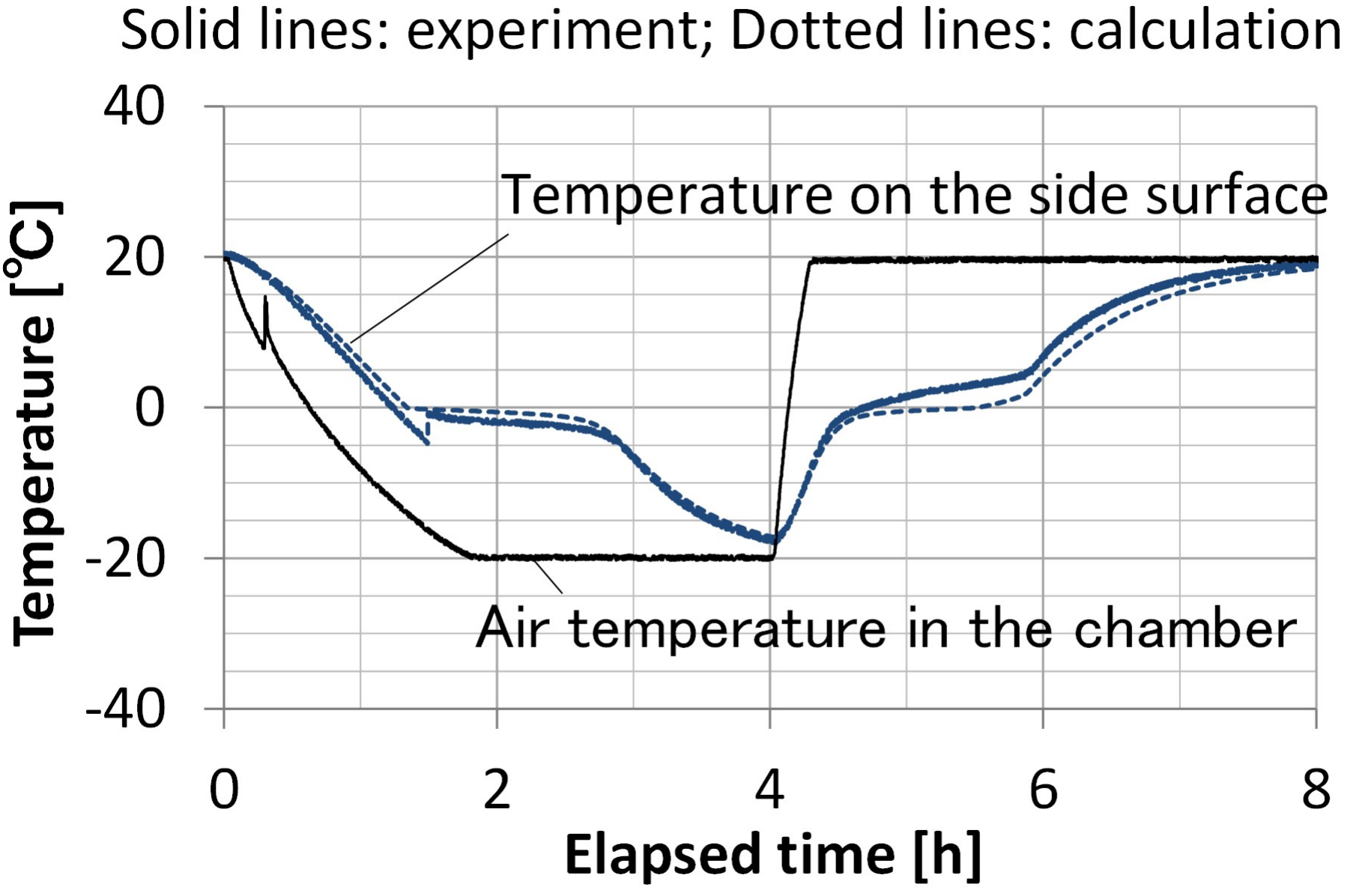
Solid lines: experiment; Dotted lines: calculation
Temperature on the side surface
Air temperature in the chamber
Temperature [°C]
40
20
0
-20
-40
0
2
4
6
8
Elapsed time [h]

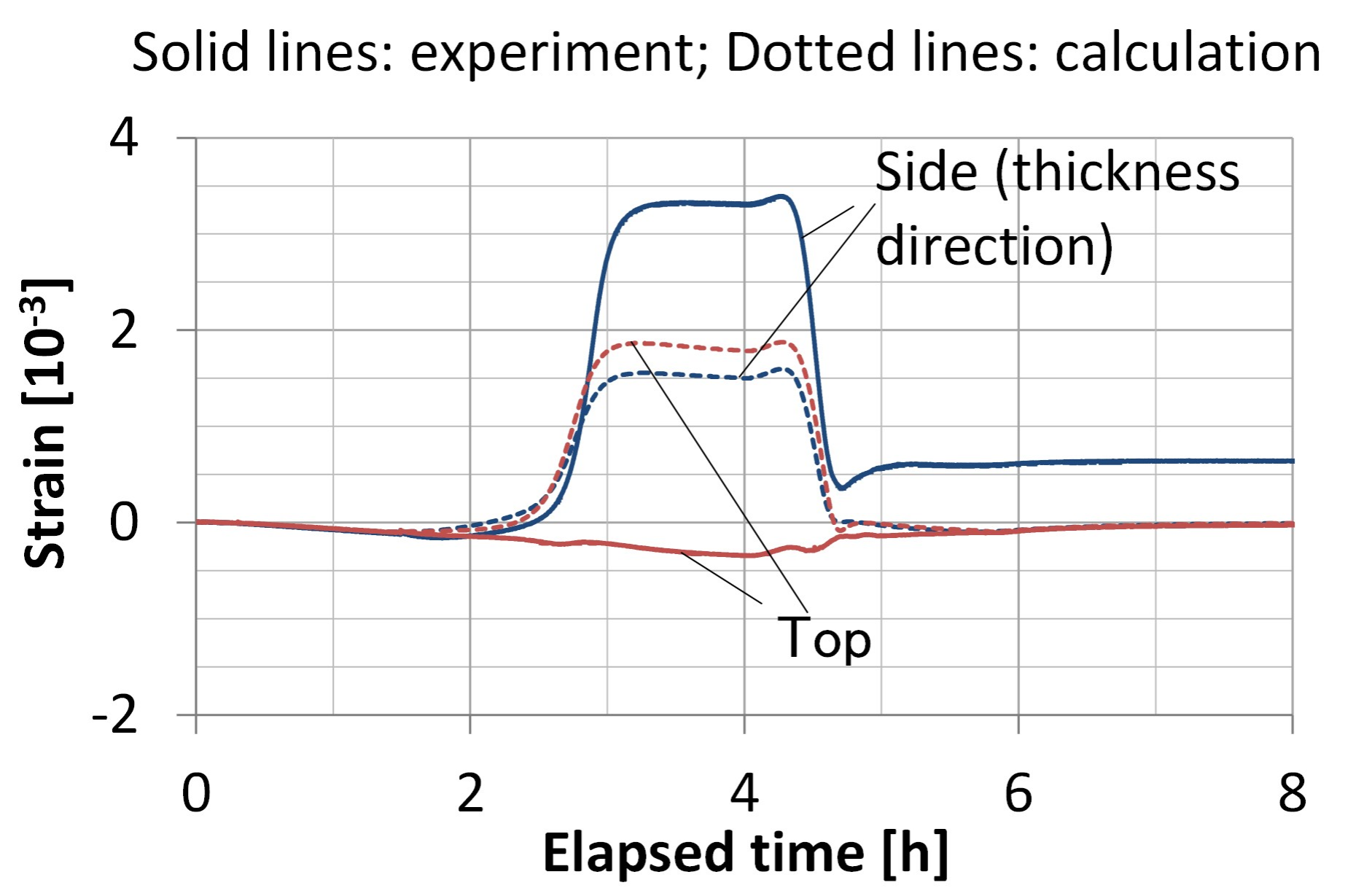
Solid lines: experiment; Dotted lines: calculation
Side (thickness direction)
Top
Strain [10-3]
Elapsed time [h]
4
2
0
-2
0
2
4
6
8

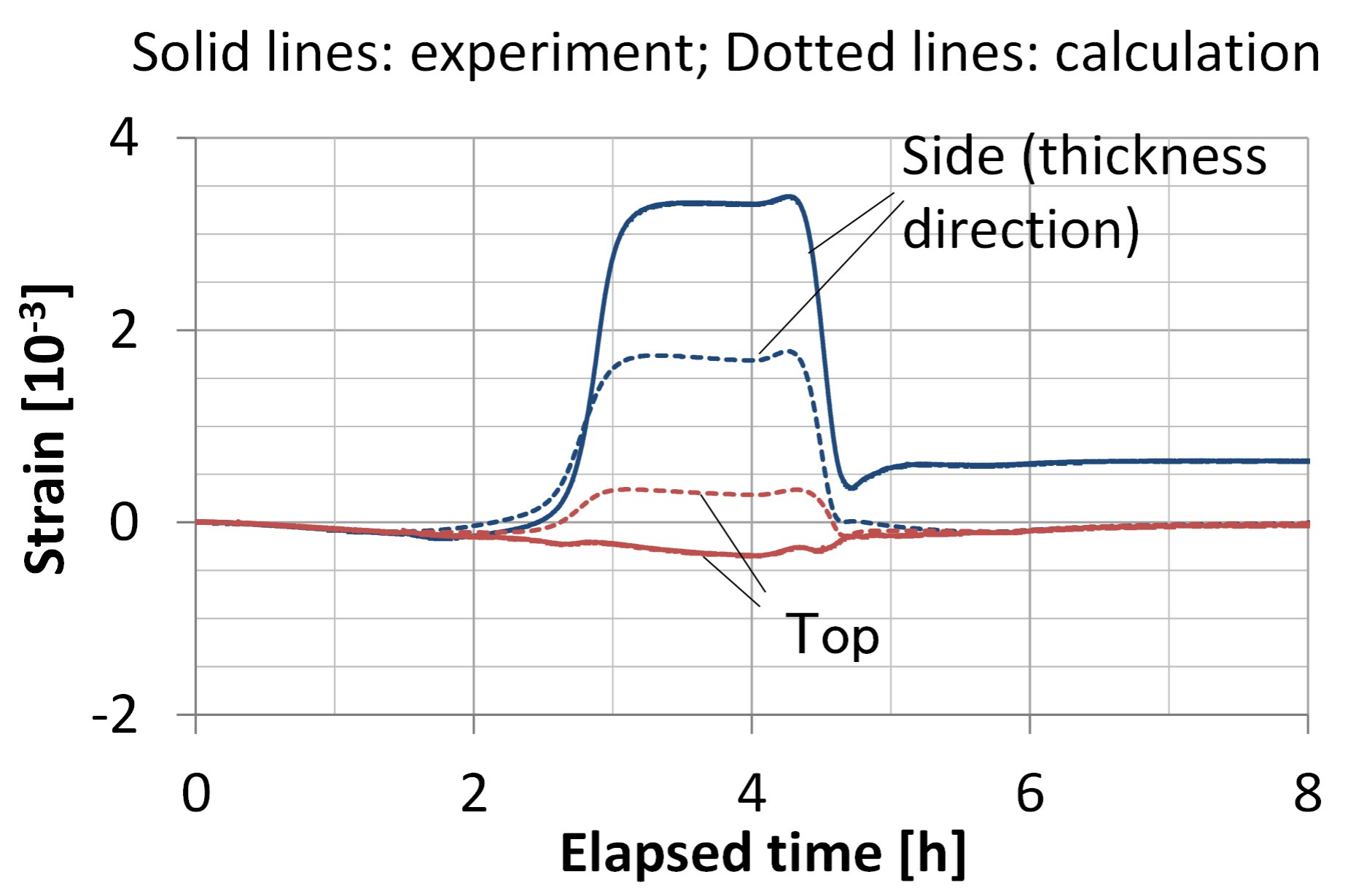
Solid lines: experiment; Dotted lines: calculation
Side (thickness direction)
Top
Strain [10-3]
Elapsed time [h]
4
2
0
-2
0
2
4
6
8

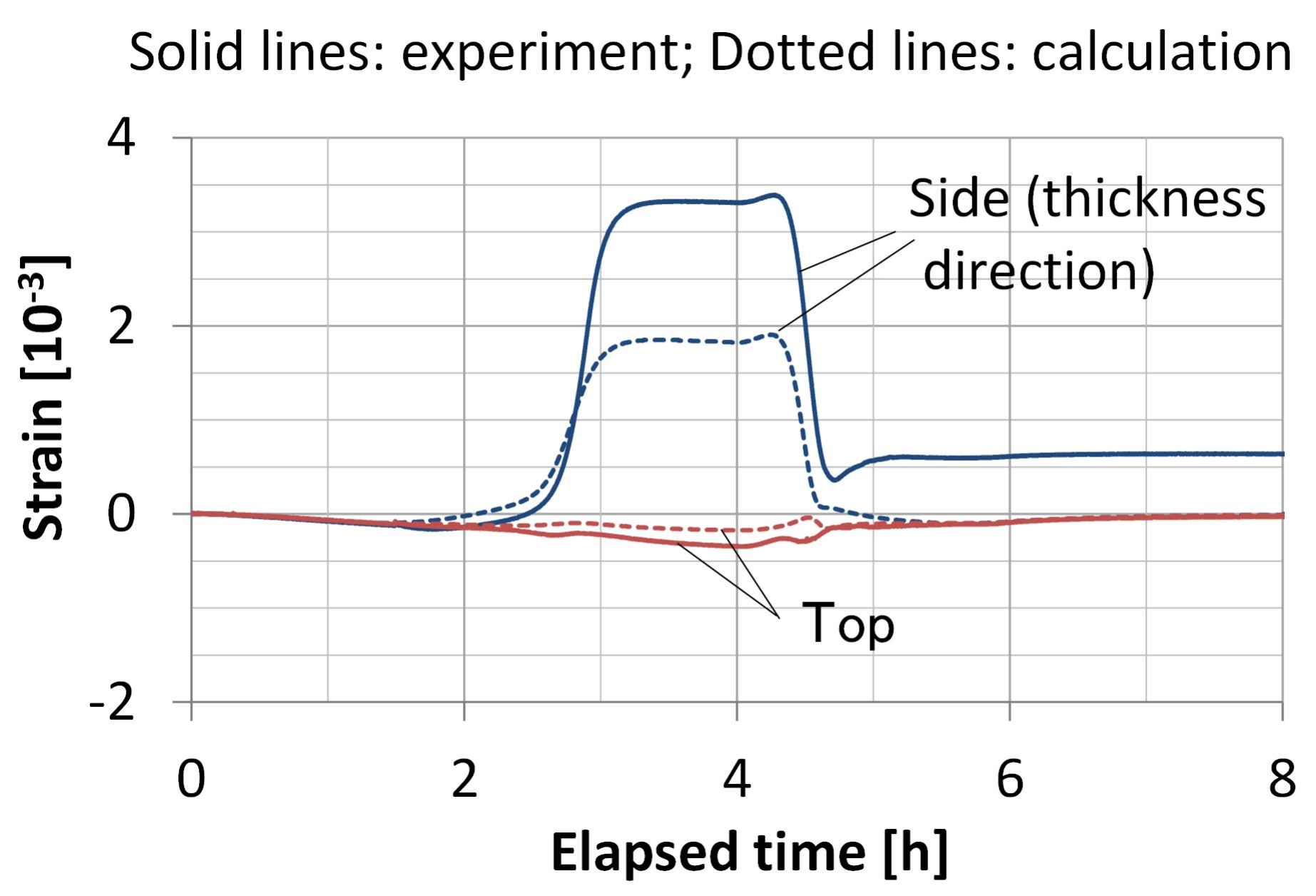
Solid lines: experiment; Dotted lines: calculation
Strain [10-3]
4
2
0
-2
Side (thickness direction)
Top
0
2
4
6
8
Elapsed time [h]

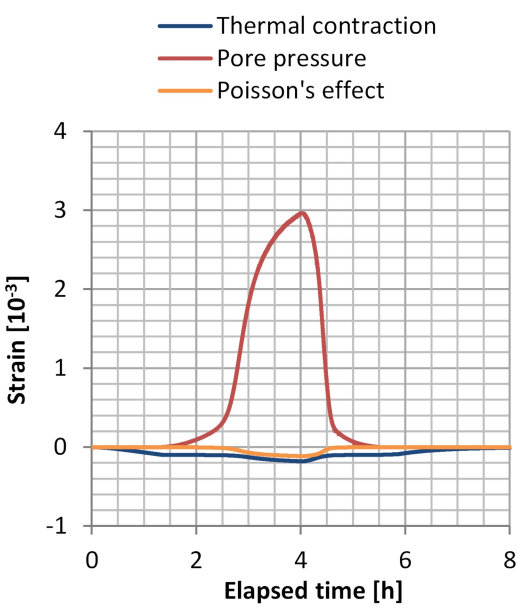
Thermal contraction
Pore pressure
Poisson's effect
Strain [10-3]
Elapsed time [h]
4
3
2
1
0
-1
0
2
4
6
8

(a)

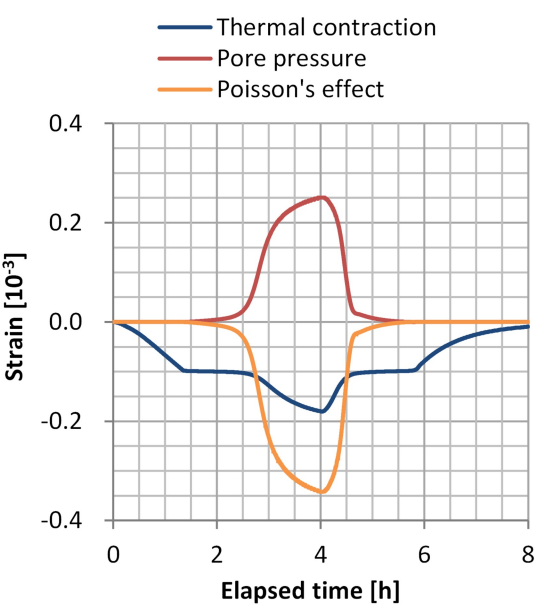
Thermal contraction
Pore pressure
Poisson's effect
Strain [10-3]
Elapsed time [h]
0.4
0.2
0.0
-0.2
-0.4
0
2
4
6
8

(b)